NASA TECHNICAL MEMORANDUM

NASA TM X- 73,154

NASA TM X- 73,154

SIMULATION OF AN AUTOMATICALLY CONTROLLED STOL AIRCRAFT IN A MICROWAVE LANDING SYSTEM MULTIPATH ENVIRONMENT

Mitsuhiko Toda, Stuart C. Brown, and Clifford N. Burrous

Ames Research Center
Moffett Field, Calif. 94035

July 1976

1. Report No.	2. Government Accession No.	3. Recipient's Catalog No.
NASA TM X-73,154		

4. Title and Subtitle	5. Report Date
SIMULATION OF AN AUTOMATICALLY-CONTROLLED STOL AIRCRAFT IN A MICROWAVE LANDING SYSTEM MULTIPATH ENVIRONMENT	6. Performing Organization Code

7. Author(s)	8. Performing Organization Report No.
Mitsuhiko Toda, Stuart C. Brown, and Clifford N. Burrous	A-6693
	10. Work Unit No. 513-53-02

9. Performing Organization Name and Address	11. Contract or Grant No.
Ames Research Center, NASA Moffett Field, California 94035	

12. Sponsoring Agency Name and Address	13. Type of Report and Period Covered
National Aeronautics and Space Administration Washington, D. C. 20546	Technical Memorandum
	14. Sponsoring Agency Code

15. Supplementary Notes

16. Abstract

This report describes the simulated response of a STOL aircraft to Microwave Landing System (MLS) multipath errors during final approach and touchdown. The MLS azimuth, elevation, and DME multipath errors were computed for a relatively severe multipath environment at Crissy Field, California, utilizing an MLS multipath simulation at MIT Lincoln Laboratory. A NASA/Ames six-degree-of-freedom simulation of an automatically-controlled deHavilland C-8A STOL aircraft was used to determine the response to these errors.

The results show that the aircraft response to all of the Crissy Field MLS multipath errors was small. The small MLS azimuth and elevation multipath errors did not result in any discernible aircraft motion, and the aircraft response to the relatively large (200-ft (61-m) peak) DME multipath was noticeable but small.

17. Key Words (Suggested by Author(s))	18. Distribution Statement
Microwave landing system Multipath effects STOL aircraft Autopilot	STAR Category - 08

19. Security Classif. (of this report)	20. Security Classif. (of this page)	21. No. of Pages	22. Price*
Unclassified	Unclassified	42	$3.75

*For sale by the National Technical Information Service, Springfield, Virginia 22161

SIMULATION OF AN AUTOMATICALLY-CONTROLLED STOL AIRCRAFT IN A MICROWAVE LANDING SYSTEM MULTIPATH ENVIRONMENT

Mitsuhiko Toda, Stuart C. Brown,
and Clifford N. Burrous

Ames Research Center

SUMMARY

This report describes the simulated response of a STOL aircraft to Microwave Landing System (MLS) multipath errors during final approach and touchdown. The MLS azimuth, elevation, and DME multipath errors were computed for a relatively severe multipath environment at Crissy Field, California, utilizing an MLS multipath simulation at MIT Lincoln Laboratory. A NASA/Ames six-degree-of-freedom simulation of an automatically-controlled deHavilland C-8A STOL aircraft was used to determine the response to these errors.

The results show that the aircraft response to all of the Crissy Field MLS multipath errors was small. The small MLS azimuth and elevation multipath errors did not result in any discernible aircraft moition, and the aircraft response to the relatively large (200-ft (61-m) peak) DME multipath was noticeable but small.

INTRODUCTION

An investigation was conducted at the NASA-Ames Research Center to determine STOL aircraft performance in a Microwave Landing System (MLS) multipath environment. The site simulated, Crissy Field, California, was selected by the International Civil Aviation Organization (ICAO) All Weather Operations Panel as a potentially difficult STOLport multipath environment due to the proximity of buildings to the runway. The MIT Lincoln Laboratory provided simulated errors for a typical MLS azimuth, elevation, and DME siting at Crissy Field (ref. 1). The NASA-Ames six-degree-of-freedom simulation of a deHavilland C-8A STOL aircraft and Automatic Flight Control System (AFCS), designed to utilize the MLS DME as well as angular information, was used to determine the aircraft response to these multipath errors. The effects of individual and combinations of MLS multipath errors were evaluated in the automatic control mode from 500 ft (152 m) altitude on the final approach to touchdown. The sensitivity of several AFCS variations to multipath errors was also determined.

SYSTEM DESCRIPTION

This section contains a brief description of the simulated STOL aircraft and pertinent portions of its flight control system, the MLS and Crissy Field siting, and the simulation conditions.

Aircraft

The STOL aircraft simulated in this study is a prototype version of the deHavilland DHC-5 (C-8A) twin-turboprop STOL transport (ref. 2) illustrated in figure 1. The simulation program used in this study is a representation of the automatic control portion of the STOLAND-piloted simulation facility on an IBM 360 computer (ref. 3). The simulation model includes the six-degree-of-freedom nonlinear aerodynamic equations of the aircraft; the kinematic and nonlinear aerodynamic equations of the aircraft; the kinematic and nonlinear aerodynamic equations of motion (ref. 4) and a General Electric T64-10 turboprop engine model. Further descriptions of the systems represented by the STOLAND facility are included in references 5 and 6.

MLS Multipath Errors and Siting

The MLS multipath errors were computed through the use of a simulation developed by MIT Lincoln Laboratory (ref. 1). This simulation represents a Time Reference Scanning Beam (TRSB) MLS with a conical coordinate system, C-band azimuth (AZ), primary elevation (EL-1) and flare elevation (EL-2), and L-band DME signals. Multipath errors are determined at the actual transmitted sampling rates (40 Hz for DME, EL-1 and EL-2, and 13.5 Hz for AZ). The data was processed by a model of the MLS airborne receiver which includes motion averaging of the signals over each output sampling period. The receiver output data rate was 5 Hz for all MLS functions. The errors were calculated at discrete points along the nominal undisturbed flight path. The STOLport MLS siting and multipath environment used for this study are shown in figures 2 and 3. The simulated buildings are based on actual Crissy Field locations and represent a potentially severe multipath environment due to the closeness of these structures to the runway and MLS antennas. Some of these structures are located above the transitional surface specified by the STOLport design criteria (ref. 7) as shown in figure 2(b).

Control and Navigation Systems

The aircraft control system functions are simulated on an IBM 360 computer in a manner similar to that programmed in the airborne digital computer so that the fixed-point computational accuracies in the airborne computer are preserved. The sensing and frequency ranges used are comparable with present-day advanced autopilots; however, this AFCS is designed to use all of the MLS information including DME. Although the simulation is capable of representing various modes of automatic flight in the terminal area (refs. 5 and 6), the

simulation results in this report are limited to the final portion of the glidepath, flare and touchdown.

Only those portions of the AFCS system which interact with the multipath disturbances and result in aircraft motions will be described.

The pertinent STOLAND navigation and longitudinal control systems are illustrated in figure 4. The details of each subsystem are described in appendix A. In addition to the basic AFCS described in figure 4, an alternate glide-slope tracking system, which is intended to be less sensitive to DME noise, was simulated (see fig. 20, appendix A). The separate glide-slope tracking filter obtains filtered glide-slope error and rate directly from the calculated error relative to the nominal glide slope. In the basic system, these errors are computed from the longitudinal and vertical runway-oriented position/rate estimates ($\hat{X}_R$, $\hat{Z}_R$, $\dot{\hat{X}}_R$, and $\dot{\hat{Z}}_R$ in fig. 4). Details of the differences between the two systems are described in appendix A (fig. 20), and an analysis of their sensitivity to DME noises is shown in appendix B.

Since aircraft lateral motion due to the very small azimuth multipath errors is negligible, the lateral control, localizer tracking, and roll/yaw stability augmentation systems are not shown. Similarly, since the multipath disturbances do not affect airspeed or throttle motion, the description of the autothrottle system is not included.

Simulation Conditions

All runs were made with the following conditions: a six-degree glide slope, 71-knot airspeed, aircraft in the landing configuration, and initialization of multipath errors at 500-ft (152-m) altitude.

The MLS multipath errors were calculated at discrete points along the nominal unperturbed flight path for the C-8A/STOLAND simulation to investigate their effects on aircraft motion. Note that this procedure neglects any change in the received multipath signals due to perturbations of the aircraft from the nominal path. However, this can be justified since the excursions of the aircraft due to these errors were small as shown in the following section. In order to isolate the effects of the multipath errors, no atmospheric disturbance or MLS errors other than multipath errors were simulated.

SIMULATION RESULTS

The glide-slope tracking and flare results are discussed separately.

Glide-Slope Tracking

Simulation with the Basic C-8A/STOLAND System- The Crissy Field multipath errors, supplied by the Lincoln Laboratory, are shown in figure 5. A detailed analysis of these errors is included in reference 1. Note that the MLS

azimuth multipath errors are negligible (<0.001° peak-to-peak), and the only significant elevation multipath error is negative 0.02° spike at ≅43 sec which is caused by Building B-5 (fig. 2). The DME errors are initially small but gradually increase. A small positive DME bias and several cyclic negative spikes of ≅200 ft (61 m) maximum amplitude occur near the threshold. These spikes are apparently caused by Building B-1 (fig. 2). Multipath errors during the flare will be discussed in the section on Flare and Touchdown.

The response of the aircraft is shown in figures 6 through 9 for the following sets of multipath errors:

figure 6 (run 1): No MLS errors
figure 7 (run 2): MLS Elevation (EL-1) multipath errors only
figure 8 (run 3): MLS DME multipath errors only
figure 9 (run 4): MLS EL-1 and DME multipath errors

Generally, the plotted results are shown with expanded scales so that the relatively small aircraft motions are apparent. For the data with double lines, the right scales correspond to solid data lines and left scales correspond to the dashed data. (This is true for both systems of units shown.) The lateral response of the aircraft to the very small azimuth errors (<0.0006 deg) was negligible, and hence the aircraft's lateral response results are not shown.

Time statistics and maximum values of selected aircraft parameters, which represent the incremental effect of the multipath disturbances are summarized in table 1. The incremental data for a particular run were computed as the difference between the response with (run 2, 3, or 4) and without (run 1) the multipath disturbance. The statistical averages were computed for the flight-time interval for which multipath errors were determined (t = 10.8 sec to t = 46.9 sec).

The response of the aircraft to angular multipath errors was negligible. As was previously noted, the very small MLS azimuth errors do not cause any noticeable aircraft lateral motions. Figure 7 and run 2 of table 1 show that the MLS elevation multipath also does not cause any noticeable motion. Even the effects of the small elevation multipath spikes near the CAT I decision height (t = 43 sec) are filtered out by the airborne system.

The response of the aircraft to the DME multipath is noticeable but small (fig. 8 and run 3 of table 1). The maximum perturbations (table 1, run 3) show that the maximum deviation from the glide slope due to the DME multipath is 0.6 ft (0.2 m). This value is small compared to the CAT II decision height indicated vertical window of ±12 ft (3.7 m), 2σ (ref. 4). The peak vertical acceleration 0.4 ft/sec^2 (0.11 m/sec^2 = 0.012 g), with a frequency of approximately 1/3 Hz, is below any of the passenger comfort criteria tested or proposed in ref. 8. For instance, it is below the 0.1 g (rms) objectional acceleration level and roughly the same as the 0.015 g (peak) perceptible level reported for large transport aircraft in reference 9.

The DME multipath errors affect the vertical aircraft motions because the STOLAND autopilot utilizes DME to augment glide-slope angle tracking error

during the final approach phase as shown in figure 17.[1] (See appendix A for the explanation of fig. 17). That is, a gain scheduling function, slant range (η_{td}), and a vertical velocity damping term ($\hat{\dot{Z}}_R$) are used. Although not shown in detail, the DME errors propagate into the aircraft vertical motions mainly through the calculation of estimated $\hat{\dot{Z}}_R$, then inertial flight path angle (γ_I), and hence pitch command (θ_c) as shown in the glide-slope tracking control law of figure 17. An examination of the DME multipath errors of fig. 5 indicates two forms of disturbance: (1) a slowly increasing positive bias which is present for most of the approach path, and (2) a series of spikes which occur during the latter portion of the path. An examination of the aircraft response indicates that the aircraft is equally sensitive to both forms of disturbance.

Simulation with densitized guidance systems- In order to examine the sensitivity of the basic airborne system to the DME errors, two runs were made with gain changes in the navigation filters and the glide-slope tracking portion of the autopilot, respectively.

In the first change the cut-off frequencies of the navigation filters were lowered by a factor of 0.7. The damping ratios were also slightly changed. See appendix A for the comparison of the frequency responses of the original and desensitized filters. Figure 10 shows the aircraft response with this navigation filter modification, and time statistics for this run (run 5) are included in table 1. Comparison of figure 10 to figure 8 (run 5 and run 3 of table 1) shows a reduction in the aircraft accelerations, rates and elevator deflection; however, the position deviations are approximately doubled.

The second simulation modification involved desensitizing the autopilot (with the nominal navigation filters). The proportional gain K_p and the derivative gain K_D in figure 17 were reduced by a factor of 0.75 and 0.5, respectively, while the integral gain K_I remained the same. The results of this modification are shown in figure 11 and run 6 of table 1. This data shows that some improvement is obtained relative to the basic system of run 3; however, the amount of improvement is not significant considering the small response of run 3.

Simulation with alternate glide-slope tracking system- Although the effect of DME multipath errors on the aircraft performance was small, the alternate glide-slope tracking scheme was investigated in order to see what further improvements in performance could be made. This scheme, which utilized a glide-slope tracking filter (fig. 20) is intended to reduce effects of DME noise resulting from any source. The filter has also been tested with other types of DME errors, and has resulted in a better tracking performance than the basic system.

The simulated results of figure 12 and run 7 of table 1 show the reduction in aircraft perturbations due to the DME errors compared to the basic AFCS of figure 8 and run 3 of table 1. The superior performance of this system is primarily due to the reduction of DME error propagation into the

[1]Present-day autopilots utilize signals other than the DME to augment the glide-slope tracking error signal; hence, these systems would not be affected by DME multipath.

estimated vertical velocity and hence into the glide-slope tracking command (appendix B).

Flare and Touchdown

The multipath errors during flare are shown in figure 5. The azimuth multipath errors during flare are larger than those on the glide slope. These errors are due to the reflection of sidelobes from the structure B7 (train, fig. 2). The magnitude of the errors, however, is still small (maximum 0.0024°), and since the larger errors occur just before touchdown (duration less than 2 sec), the automatically controlled aircraft does not respond to these errors. The flare (EL-2) multipath errors are small on the glide slope (maximum magnitude 0.0076°). The EL-2 errors monotonically increase near touchdown to a maximum of 0.09°. This increase, however, occurs during the last second, and hence does not cause any noticeable aircraft perturbation. The large multipath errors during the last second are mainly caused by the ground reflection, since the EL-2 antenna (bore center height = 15 ft (4.6 m), fig. 2) is looking down toward the aircraft (height 10 ft (3 m)).

The response of the aircraft without MLS multipath errors (run 8) and with DME multipath errors (run 7) is shown in figures 13 and 14, and summarized in table 2. The alternate glide-slope tracking system was used during glide-slope tracking for these simulations. The effects of the azimuth, elevation (EL-1) and flare (EL-2) multipath errors are negligible, and hence the data for the runs with these errors are not included.

An examination of the results shows that the relative importance of the multipath errors during flare is the same as was observed during glide-slope tracking; that is, the effects of MLS azimuth and elevation (both EL-1 and EL-2) angle multipath on aircraft motion are negligible, whereas the DME errors result in noticeable but small motions. The DME errors can affect touchdown accuracy both by altering conditions at flare initiation (end of glide-slope tracking), and by further modifying motion during the flare because of estimation errors. However, while not separately shown, the DME errors during flare did not alter the aircraft motion significantly so that changes at touchdown are due primarily to changes at flare initiation height. As shown in table 2, the DME multipath errors cause the longitudinal touchdown to vary by 23 ft (7 m), which is a small percentage of 700 ft (213 m), 2σ total allowable STOL longitudinal dispersion suggested in reference 6.

CONCLUSIONS

The simulation results show that, during the final approach and flare, the response of an automatically controlled C-8A STOL aircraft to the MLS multipath at Crissy Field, California is as follows:

Neither the azimuth nor elevation (EL-1/EL-2) multipath affects the aircraft response. The response of the aircraft to the relatively large DME multipath [200 ft (61 m) peak] is noticeable but small. For instance, during

glide-slope tracking, the maximum aircraft deviation from the glide slope is only 0.7 ft (0.2 m), the maximum vertical acceleration is 0.012 g, and the maximum pitch angle change is 0.34°.

ACKNOWLEDGMENT

The authors would like to express their gratitude to Dr. Tsuyoshi Goka for his valuable suggestions and Flora Watson for her help in computer programming.

APPENDIX A

DESCRIPTION OF CONTROL AND NAVIGATION SYSTEMS

The pertinent STOLAND navigation and longitudinal control subsystems illustrated in figure 4 are described in this section.

Navigation Filtering

The navigation filters used in this study are fixed parameter complementary filters that are intended for use with a variety of navigation aids and control system modes. The filters combine resolved accelerometer information with MLS derived position information given in a runway-referenced rectangular coordinate system (X'_R, Y'_R, and Z'_R in fig. 4). In the basic system, the calculated altitude (derived from DME and EL-1 signals) is processed by a second order filter to obtain estimated altitude and rate for glide-slope tracking. A separate altitude calculation using the EL-2 signal is blended into a second vertical filter between 400 and 200 ft (122 and 61 m) altitude to provide estimates during flare.

The filter block diagrams are given in figure 15. The transfer functions for position estimates are given by

Horizontal Filter

$$H_H(S) = \frac{\hat{X}_R(S)}{X'_R(S)} = \frac{\hat{Y}_R(S)}{Y'_R(S)} = \frac{0.4(S^2 + 2\zeta_3\alpha_3 S + \alpha_3^2)}{(S + \alpha_1)(S^2 + 2\zeta_2\alpha_2 S + \alpha_2^2)} \tag{1}$$

$$\alpha_1 = 0.2, \quad \alpha_2 = 0.14, \quad \alpha_3 = 0.1$$

$$\zeta_2 = 0.7, \quad \zeta_3 = 0.75$$

Vertical Filter

$$H_V(S) = \frac{\hat{Z}_R(S)}{Z'_R(S)} = \frac{0.65(S + \alpha_5)}{S^2 + 2\zeta_4\alpha_4 S + \alpha_4^2} \tag{2}$$

$$\alpha_4 = 0.42, \quad \alpha_5 = 0.27, \quad \zeta_4 = 0.78$$

X'_R, Y'_R, Z'_R: Position derived from MLS measurements

$\hat{X}_R$, $\hat{Y}_R$, $\hat{Z}_R$: Position estimates

Note that the horizontal channel consists of three integrators whereas the vertical channel involves two. The gains for the filters are based on flight test experience with the STOLAND system.

For the desensitized navigation filters (discussed under Simulation Results - Glide-Slope Tracking), the cutoff frequencies are reduced so that their transfer functions are expressed by

$$H_H(S) = \frac{3\alpha_H S^2 + 3\alpha_H^2 S + \alpha_H^3}{(S + \alpha_H)^3} \quad \text{(Horizontal Filters)}$$

$$H_V(S) = \frac{2\alpha_V S + \alpha_V^2}{(S + \alpha_V)^2} \quad \text{(Vertical Filters)}$$

where the cut-off frequencies are $\alpha_H = 0.1$, $\alpha_V = 0.3$. Figure 16 shows the original and desensitized navigation filter frequency responses ($H_H(S)$ and $H_V(S)$). Figure 16 also gives the response of the corresponding transfer functions between derivatives of MLS measurements and rate estimates ($\hat{X}_R(s)/sX'_R(s)$, etc.).

Glide-Slope Tracking Control

The glide-slope tracking law illustrated in figure 17 is expressed by the following equations.

Pitch Command

$$\theta_C = K_P\eta_{TD}\beta_{GS} + K_D\,(\gamma_{REF} - \gamma_I) \tag{3}$$

$$K_P = \frac{32}{360}, \quad K_D = 1, \quad \gamma_{REF} = 6^\circ$$

Pitch Integral Command

$$\theta_{CI} = K_I \int \eta_{TD}\beta_{GS}, \quad K_I = \frac{1}{360} \tag{4}$$

$$\eta_{TD} = \sqrt{\hat{X}_R^2 + \hat{Y}_R^2 + \hat{Z}_R^2} \quad : \text{ Slat range to touchdown}^2 \qquad (5)$$

$$\beta_{GS} = \gamma_{REF} - \tan^{-1}\left(\frac{\hat{Z}_R}{\hat{X}_R}\right) \quad : \text{ Planar glide-slope deviation}^2 \qquad (6)$$

$$\gamma_I = \tan^{-1}\left(\frac{\hat{Z}_R}{\sqrt{\hat{X}_R^2 + \hat{Y}_R^2}}\right) \quad : \text{ Inertial flight-path angle}^2 \qquad (7)$$

The vertical position error from the nominal glide slope ($\eta_{TD}\beta_{GS}$) is computed from position estimates ($\hat{X}_R$, $\hat{Y}_R$ and $\hat{Z}_R$) and used to provide proportional and integral terms of the glide-slope tracking law. The rate estimates $\dot{\hat{X}}_R$, $\dot{\hat{Y}}_R$ and $\dot{\hat{Z}}_R$) are used to calculate the vertical flight path angle γ_I and provide a derivative term in the control law.

Flare Control

Filtered altitude and altitude rate derived from the flare (EL-2) antenna signals are used to initiate flare and determine flare control during the flare. Altitude rate feedback is used based on a calculated rate command. A predictive command is also added since feedback control alone is not sufficient to generate the required change from the six-degree glide slope to the desired sink rate at touchdown.

The flare laws are illustrated in figure 18 and summarized by the following equations.

Flare Initiation Law

$$\hat{Z}_R + \tau_P \dot{\hat{Z}}_R < Z_F$$

$$\tau_P = 2.0 \text{ sec}, \quad Z_F = 19.0 \text{ ft (5.8 m)}$$

---

[2]Although the data presented in this report are expressed in the coordinate system given in figure 2, the rectangular coordinate system implemented in the airborne computer is as follows (ref. 4). Its origin and polarities are defined by the following sketch.

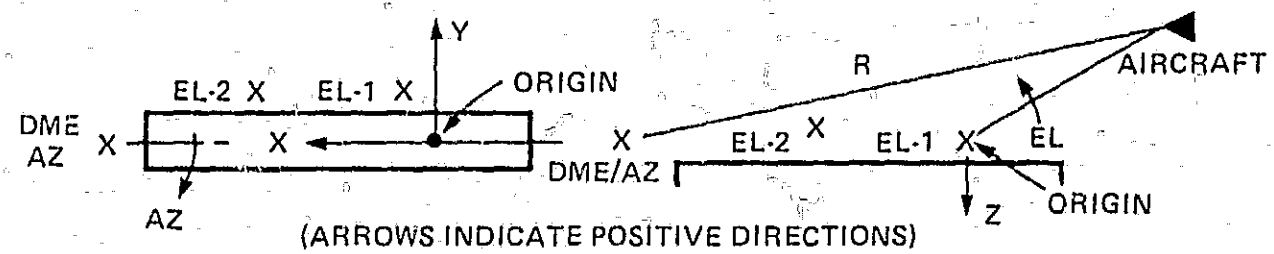

Flare Control Law

Pitch Command (Closed Loop Command)

$$\theta_C = K_{PF}\dot{Z}_e + K_{IF}\int \dot{Z}_e + K_{DF}\ddot{Z}_R$$

$$K_{PF} = 5/4 \ , \quad K_{IF} = 1/4 \ , \quad K_{DF} = -3/4$$

$$\dot{Z}_e = \dot{Z}_{CMD} - (\hat{\dot{Z}}_R + \dot{Z}_{TD})$$

$$\dot{Z}_{CMD} = [\hat{\dot{Z}}_R(t_o) + \dot{Z}_{TD}]\exp\left(-\frac{t - t_o}{\tau_c}\right) : \text{ Exponential flare sink rate command}$$

$$\dot{Z}_{TD} = 1.5 \text{ ft/sec } (0.46 \text{ m/sec}) \ , \quad \tau_c = 1.8 \text{ sec}$$

t_o: Time of flare initiation

Predicted Pitch Command (Open Loop Command)

$$\theta_P = (\gamma_{REF} + \gamma_F)\left[1 - \exp\left(-\frac{t - t_o}{\tau_o}\right)\right]$$

$$\gamma_F = 3.9^\circ \ , \quad \tau_o = 2.0 \text{ sec}$$

A slight amount of throttle retard was used during the exponential flare maneuver to reduce the probability of long floating touchdowns.

Pitch Stability Augmentation System

The pitch commands (θ_c, θ_{cl}, θ_p) of the glide-slope tracking and flare control laws are augmented by pitch angle and angular rate feedback signals to stabilize pitch attitude. The augmentation system is illustrated in figure 19. The pitch rate measurement is fed through a washout filter to suppress steady-state rates during turns.

Glide-Slope Tracking Filter

For the alternate glide-slope tracking system, a glide-slope tracking filter was implemented to reduce the effect of DME errors during glide-slope tracking. Figure 20 illustrates the difference between the two systems in estimating the altitude error, Δh, from the nominal glide slope.

The glide-slope tracking filter has the same structure and gains as the vertical filter in figure 15. However, its MLS position input is the measured altitude error from the nominal glide slope calculated by

$$\Delta h' = Z'_R - (\tan \gamma_{REF})X'_R - ZEL \qquad (8)$$

where ZEL is the height of EL-1 antenna. Its outputs, estimated altitude error ($\hat{\Delta h}$) and error rate ($\hat{\dot{\Delta h}}$), are utilized in the modified glide-slope tracking law:

$$\theta_C = K_P \hat{\Delta h} + K_{DD} \hat{\dot{\Delta h}} \tag{9}$$

$$K_P = \frac{32}{360}, \quad K_{DD} = \frac{1}{120}$$

$$\theta_{CI} = K_I \int \hat{\Delta h} \tag{10}$$

$$K_I = \frac{1}{360}$$

Note that this law is equivalent to the basic glide-slope tracking law of equations (3) and (4). $\hat{\Delta h}$ and $\hat{\dot{\Delta h}}$ in equations (9) and (10) are equivalent to $\eta_{TD}\beta_{GS}$ and $(\gamma_{REF} - \gamma_I)$ in equations (3) and (4). The difference in the derivative gain K_{DD} in equation (9) versus K_D in equation (3) is due to the difference in dimensions between $\hat{\dot{\Delta h}}$ and $(\gamma_{REF} - \gamma_I)$.

APPENDIX B

ANALYSIS OF DME ERROR REDUCTION IN THE GLIDE-SLOPE TRACKING FILTER

The improvement of the glide-slope tracking performance in the presence of DME errors with the glide-slope tracking filter (see Simulation Results) is primarily due to the reduction of DME noise propagation into the damping term of the glide-slope tracking law. This section contains an analysis of the improvement.

The equations for the conical to rectangular coordinate conversion in the airborne computer are (fig. 4)

$$Y'_R = -R' \sin AZ'$$

$$X'_R = (B - \sqrt{B^2 - AC})/A$$

$$Z'_R = ZEL - \sqrt{X'^2_R + (Y'_R - YEL)^2} \tan EL'$$

where

$$A = 1 + \tan^2 EL'$$

$$B = XDME$$

$$C = XDME^2 + Y'^2_R + (Y'_R - YEL)\tan^2 EL' - R'^2 \cos^2 AZ'$$

XDME: X position of the DME antenna

YEL: Y position of the EL-1 antenna

ZEL: Z position of the EL-1 antenna

During glide-slope tracking, the lateral motions and azimuth errors are small so that

$$AZ' \cong 0 \ , \quad Y'_R \cong 0 \quad \text{and} \quad |YEL| << |X'_R|$$

Furthermore, since $EL' \cong \gamma_{REF} = 6°$

$$\tan^2 EL' \cong 0.01 \cong 0$$

Therefore, X'_R and Z'_R are approximated by

$$X'_R \cong XDME - (R + \Delta R)$$

$$-Z'_R \cong (\tan EL')(R + \Delta R - XDME) - ZEL \qquad (11)$$

where ΔR is the DME measurement noise. With the above approximations, equation (8) becomes

$$\Delta h' \cong (\tan EL' - \tan \gamma_{REF})(R + \Delta R - XDME) \qquad (12)$$

Differentiating equations (11) and (12), and rearranging with the approximation $\tan EL' \cong EL'$

$$\dot{Z}'_R \cong EL' \cdot \dot{\Delta R} + EL' \cdot \dot{R} + \dot{EL}'(R + \Delta R - XDME) \qquad (13)$$

$$\dot{\Delta h}' \cong \varepsilon \cdot \dot{\Delta R} + \varepsilon \cdot \dot{R} + \dot{EL}'(R + \Delta R - XDME) \qquad (14)$$

where $\varepsilon = EL' - \gamma_{REF}$.

A comparison of equations (13) and (14) explains the reduced sensitivity to DME noise for the alternate glide-slope tracking system with the glide-slope tracking filter. The error due to higher frequency DME noise, $\dot{\Delta R}$, at the input of the glide-slope tracking filter is significantly smaller than that at the basic vertical filter. This is because the $\dot{\Delta R}$ multiplication factor in equation (14) (ε) is much smaller than the factor in equation (13) (EL'). Since the same vertical filter is used for each system, the same relative magnitudes of DME errors propagate into the rate estimates, $\hat{\dot{Z}}_R$ and $\hat{\dot{\Delta h}}$, and hence, into the glide-slope tracking laws (eqs. (3) and (9)).

REFERENCES

1. Shnidman, D. A.: MLS Multipath Errors for Four Representative Airport Environments, MIT Lincoln Laboratory ATC Working Paper 44WP-5022, September 1975.

2. Taylor, J. W. R. (ed): Jane's All the World's Aircraft 1968-1969, McGraw-Hill, New York, 1969.

3. Karmakar, J. S. and Kareemi, M. N.: Organization and Use of a Software/Hardware Avionics Research Program (SHARP), NASA CR-137676, July 1975.

4. McFarland, R. E.: A Standard Kinematic Model for Flight Simulation at NASA-Ames, NASA CR-2497, 1975.

5. Young, L. S.; Hansen, Q. M.; Rouse, W. E. and Osder, S. S.: Development of STOLAND, a Versatile Navigation, Guidance and Control System, NASA TM X-62,183, 1972.

6. Burrous, C. N.; Brown, S. C.; Goka, T. and Park, K. E.: Microwave Landing System Requirements for STOL Operations, AIAA J. Aircraft, vol. 13, 1976, pp. 140-148.

7. Anon.: Planning and Design Criteria for Metropolitan STOLports, FAA Advisory Circular 150/5300-8, November 5, 1970.

8. Proceedings of Symposium on Vehicle Ride Quality, NASA TM X-2620, 1972.

9. Holloway, R. B.; Brumaghin, S. H.: Tests and Analyses Applicable to Passenger Ride Quality of Large Transport Aircraft, NASA TM X-2620, 1972, pp. 91-113.

TABLE 1.- SUMMARY OF AIRCRAFT DEVIATIONS ON GLIDE SLOPE DUE TO MULTIPATH

(a) Maximum deviations

AIRCRAFT PARAMETERS		RUN NO. (MULTIPATH ERRORS)					
		2(EL)	3(DME)	4(EL & DME)	5(DME)	6(DME)	7(DME)
ELEVATOR ANGLE,	deg	0.1	0.8	0.8	0.6	0.5	0.3
VERTICAL ACCEL., (BODY AXIS)	ft/sec^2 (m/sec^2)	0.0 (0.01)	0.4 (0.11)	0.4 (0.11)	0.3 (0.08)	0.2 (0.07)	0.1 (0.04)
SINK RATE,	ft/sec (m/sec)	0.0 (0.00)	0.5 (0.14)	0.5 (0.15)	0.2 (0.06)	0.3 (0.08)	0.1 (0.02)
ALTITUDE ERROR FROM GLIDE SLOPE,	ft (m)	0.0 (0.00)	0.6 (0.20)	0.7 (0.20)	1.4 (0.43)	0.4 (0.12)	0.2 (0.05)
PITCH RATE,	deg/sec	0.0	0.4	0.4	0.3	0.2	0.1
PITCH ANGLE,	deg	0.0	0.3	0.4	0.2	0.2	0.1
LONGITUDINAL ACCEL., (BODY AXIS)	ft/sec^2 (m/sec^2)	0.0 (0.00)	0.1 (0.04)	0.1 (0.04)	0.1 (0.03)	0.1 (0.03)	0.0 (0.01)
GROUND SPEED PARALLEL TO RUNWAY,	ft/sec (m/sec)	0.0 (0.00)	0.1 (0.04)	0.1 (0.04)	0.1 (0.03)	0.1 (0.02)	–
SLANT RANGE TO GPIP	ft (m)	0 (0.0)	1 (0.3)	1 (0.3)	2 (0.5)	1 (0.3)	1 (0.2)

RUN 2, 3 AND 4 : SIMULATION WITH BASIC STOLAND SYSTEM
RUN 5 : SIMULATION WITH DESENSITIZED NAVIGATION FILTERS
RUN 6 : SIMULATION WITH DESENSITIZED AUTOPILOT
RUN 7 : SIMULATION WITH GLIDE-SLOPE TRACKING FILTER

NOTE: THE DATA FOR AIRCRAFT PARAMETERS ARE INCREMENTAL VALUES COMPUTED AS THE VALUE FOR EACH RUN MINUS NO MULTIPATH ERROR CASE (SEE SECTION III)

TABLE 1.- CONCLUDED

(b) Mean and standard deviation of time statistics

STATISTICS / VARIABLES		MEAN						STANDARD DEVIATION					
MLS MULTIPATH ERRORS	AZIMUTH, deg	-3.1×10^{-6}						1.7×10^{-4}					
	ELEVATION, deg	-2.4×10^{-4}						0.0018					
	DME, ft(m)	8.7 (2.7)						49 (14.9)					
RUN NO. (MULTIPATH ERRORS)		2(EL)	3(DME)	4 (EL & DME)	5(DME)	6(DME)	7(DME)	2(EL)	3(DME)	4 (EL & DME)	5(DME)	6(DME)	7(DME)
AIRCRAFT PARAMETERS	ELEVATOR ANGLE, deg	$1.6X10^{-4}$	-0.0055	-0.0066	0.0028	0.0056	-0.0061	0.013	0.23	0.23	0.16	0.13	0.071
	VERTICAL ACCEL., (BODY AXIS) ft/sec^2 (m/sec^2)	$7.1X10^{-5}$ ($2.2X10^{-5}$)	-0.013 (-0.0040)	-0.013 (-0.0040)	-0.0057 (-0.0017)	-0.0070 (-0.0021)	0.0016 (0.00049)	0.0025 (0.00076)	0.16 (0.049)	0.16 (0.049)	0.11 (0.034)	0.091 (0.028)	0.033 (0.010)
	SINK RATE, ft/sec^2 (m/sec^2)	$-3.1X10^{-4}$ ($-9.4X10^{-5}$)	0.0055 (0.0017)	0.0051 (0.0016)	0.038 (0.012)	0.0076 (0.0023)	-0.0023 (-0.00070)	0.0015 (0.00045)	0.13 (0.040)	0.13 (0.040)	0.081 (0.025)	0.072 (0.022)	0.030 (0.0091)
	ALTITUDE ERROR FROM GLIDE SLOPE, ft (m)	0.0020 (0.00061)	-0.33 (-0.10)	-0.33 (-0.10)	-0.53 (-0.16)	-0.16 (-0.049)	-0.030 (-0.0091)	0.0045 (0.0014)	0.18 (0.055)	0.18 (0.055)	0.38 (0.12)	0.13 (0.040)	0.053 (0.016)
	PITCH RATE, deg/sec	$-9.2X10^{-5}$	0.0085	0.0085	0.0054	0.0052	$1.7X10^{-4}$	0.0023	0.16	0.17	0.10	0.092	0.034
	PITCH ANGLE, deg	$1.8X10^{-4}$	0.0025	0.0030	-0.016	-0.0034	0.0075	0.0010	0.12	0.12	0.073	0.068	0.024
	LONGITUDINAL ACCEL., (BODY AXIS) ft/sec^2 (m/sec^2)	$-2.1X10^{-5}$ ($-6.4X10^{-6}$)	-0.0041 (-0.0012)	-0.0043 (-0.0013)	-0.0012 (-0.00037)	-0.0022 (-0.00067)	-0.0015 (-0.00046)	$4.6X10^{-4}$ ($1.4X10^{-4}$)	0.042 (0.013)	0.043 (0.013)	0.025 (0.0076)	0.024 (0.0073)	0.0099 (0.0030)
	GROUND SPEED PARALLEL TO RUNWAY, ft/sec (m/sec)	$-3.9X10^{-4}$ ($-1.2X10^{-4}$)	0.024 (0.0073)	0.024 (0.0073)	0.043 (0.013)	0.024 (0.0073)	–	$9.2X10^{-4}$ ($2.8X10^{-4}$)	0.045 (0.014)	0.045 (0.014)	0.030 (0.0091)	0.026 (0.0079)	–
	SLANT RANGE TO GPIP ft (m)	0.0014 (0.00043)	-0.62 (-0.19)	-0.62 (-0.19)	-0.84 (-0.26)	-0.44 (-0.13)	0.18 (0.055)	0.0038 (0.0012)	0.36 (0.11)	0.36 (0.11)	0.60 (0.18)	0.36 (0.11)	0.19 (0.058)

PEAK MLS MULTIPATH ERRORS: AZIMUTH = $5.4X10^{-4}$ deg, ELEVATION = 0.017 deg, DME 240 ft(73.2 m)

TABLE 2.- SUMMARY OF AIRCRAFT RESPONSE AT FLARE INITIATION AND TOUCHDOWN DUE TO MULTIPATH

AIRCRAFT PARAMETERS			SIMULATION RESULTS		DEVIATIONS OF RUN 7 FROM RUN 8
RUN NO. (MULTIPATH ERRORS)			8 (NONE)	7 (DME)	
FLARE INITIATION	DISTANCE FROM STOP-END OF RUNWAY,	ft(m)	2425 (739)	2413 (735)	–12 (–4)
	ALTITUDE,	ft(m)	42.9 (13.1)	41.4 (12.6)	– 1.5 (–0.5)
	GROUND SPEED PARALLEL TO RUNWAY,	ft/sec(m/sec)	120 (36.6)	120 (36.6)	0 (0)
	SINK RATE,	ft/sec(m/sec)	12.7 (3.87)	12.7 (3.87)	0 (0)
	PITCH ANGLE,	deg	–7.78	–7.73	0.05
	ALTITUDE ERROR FROM GLIDE-SLOPE,	ft(m)	0.88 (0.27)	0.61 (0.19)	– 0.27 (–0.08)
TOUCHDOWN*	DISTANCE FROM STOP-END OF RUNWAY,	ft(m)	1844 (562)	1867 (569)	23 (7)
	GROUND SPEED PARALLEL TO RUNWAY,	ft/sec(m/sec)	110 (33.5)	110 (33.5)	0 (0)
	SINK RATE,	ft/sec(m/sec)	2.44 (0.74)	2.35 (0.72)	– 0.09 (–0.02)
	PITCH ANGLE,	deg	1.83	1.82	– 0.01
DURATION OF FLARE,		sec	5.0	4.7	– 0.3

* TOUCHDOWN ALTITUDE = 10 ft (3 m)

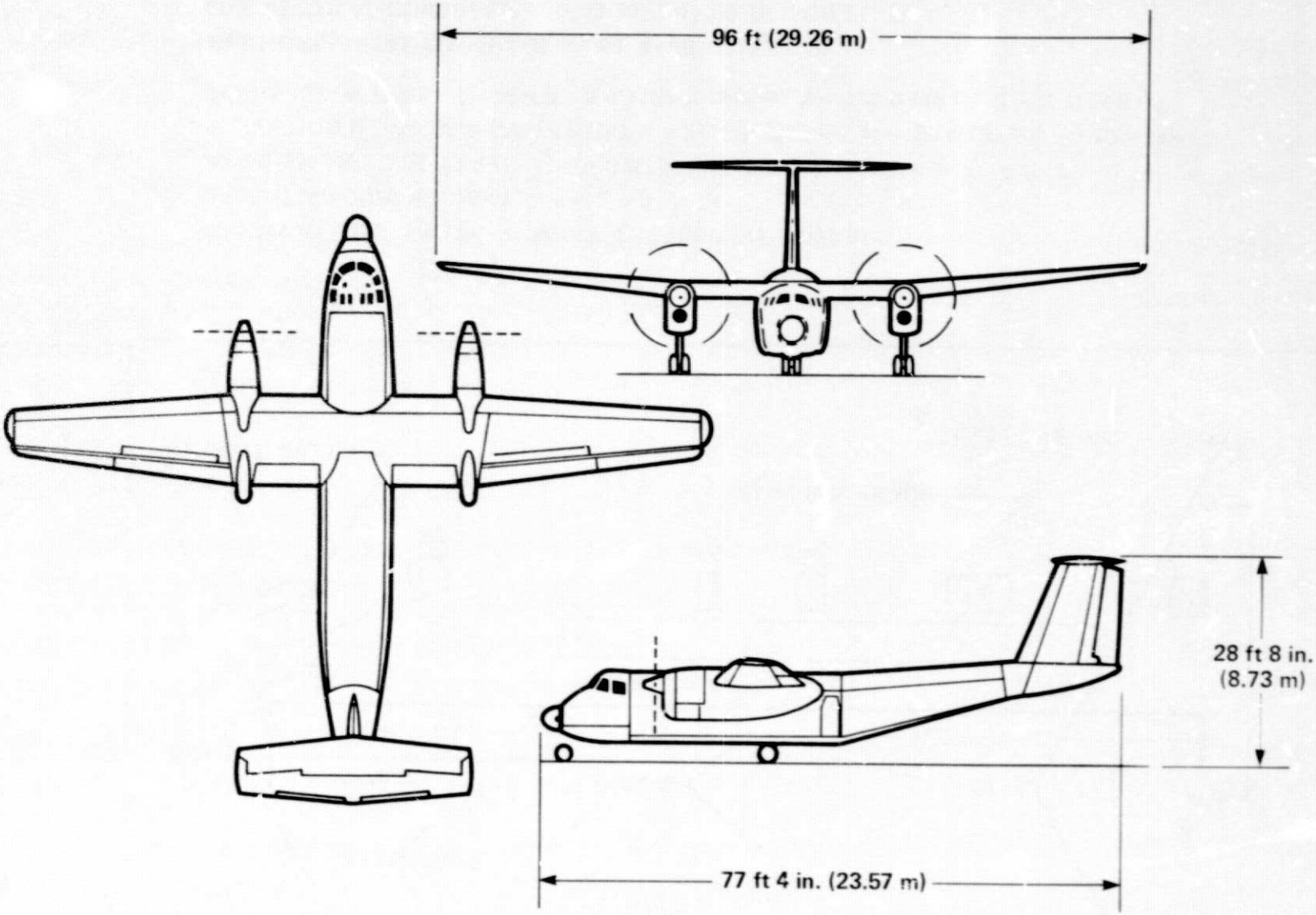

Figure 1.- C-8A (CV-7A) Buffalo Twin-Turboprop STOL Utility Transport.

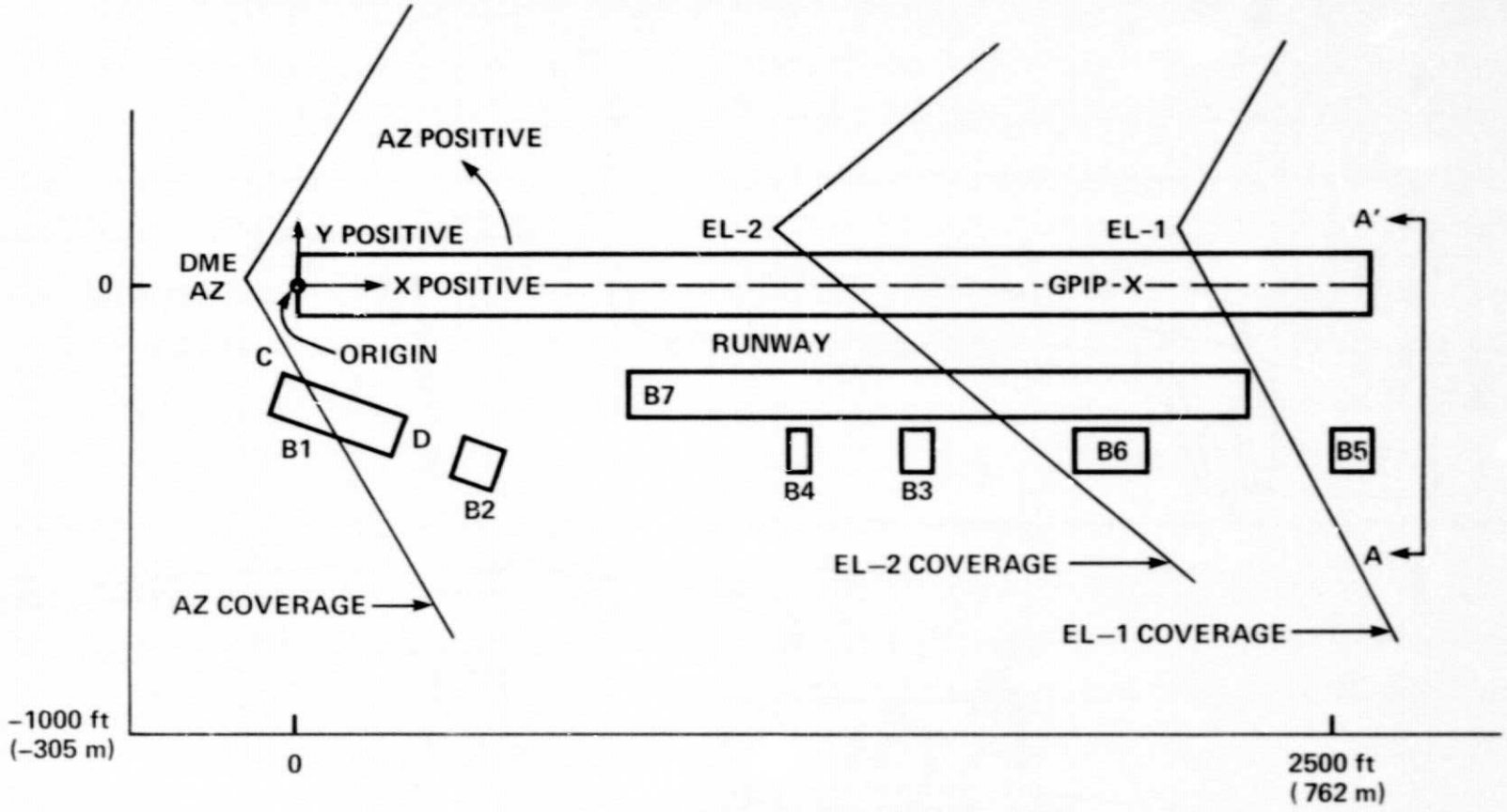

ORIGIN AT STOP-END OF RUNWAY, Z IS POSITIVE UPWARDS
GPIP AT X = 2020 ft (616 m) , Y = 0, Z = 0
AZIMUTH AND DME TRANSMITTERS AT X = -140 ft (-43 m), Y = 0, Z = 6 ft (1.8 m)
ELEVATION (EL-1) TRANSMITTER AT X = 2120 ft (646 m), Y = 120 ft (37 m), Z = 10 ft (3m)
FLARE (EL-2) TRANSMITTER AT X = 1120 ft (341 m), Y = 120 ft (37 m), Z = 15 ft (4.6 m)

MLS HORIZONTAL COVERAGE = ± 60° (± 40° FOR EL-2)
MLS VERTICAL COVERAGE = 1° TO 20° (-1° TO 10° FOR EL-2)

(a) Siting geometry

Figure 2.- Crissy Field siting.

BUILDING	LOCATION OF BUILDING FRONTS				HEIGHT	
	FROM (X, Y)		TO (X, Y)			
	ft	m	ft	m	ft	m
B1	(– 40, –200)	(–12, – 61)	(270, –290)	(82, – 88)	33	10
B2	(400, –340)	(122, –104)	(500, –370)	(152, –113)	80	24
B3	(1460, –320)	(445, – 98)	(1540, –320)	(469, – 98)	33	10
B4	(1190, –320)	(363, – 98)	(1240, –320)	(378, – 98)	33	10
B5	(2500, –320)	(762, – 98)	(2600, –320)	(792, – 98)	80	24
B6	(1880, –320)	(573, – 98)	(2060, –320)	(628, – 98)	33	10
B7 (TRAIN)	(800, –200)	(244, – 61)	(2300, –200)	(701, – 61)	16	4.9

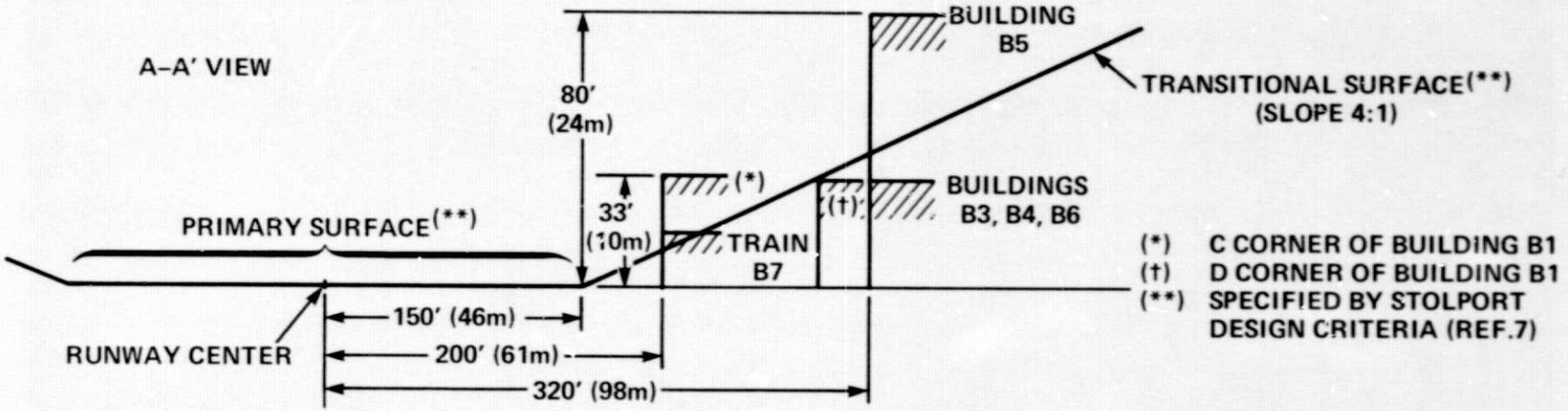

(b) Building location data and comparison with STOLport design criteria

Figure 2.- Concluded.

Figure 3 - Aerial photograph of Crissy Field (taken from the stop end of the runway).

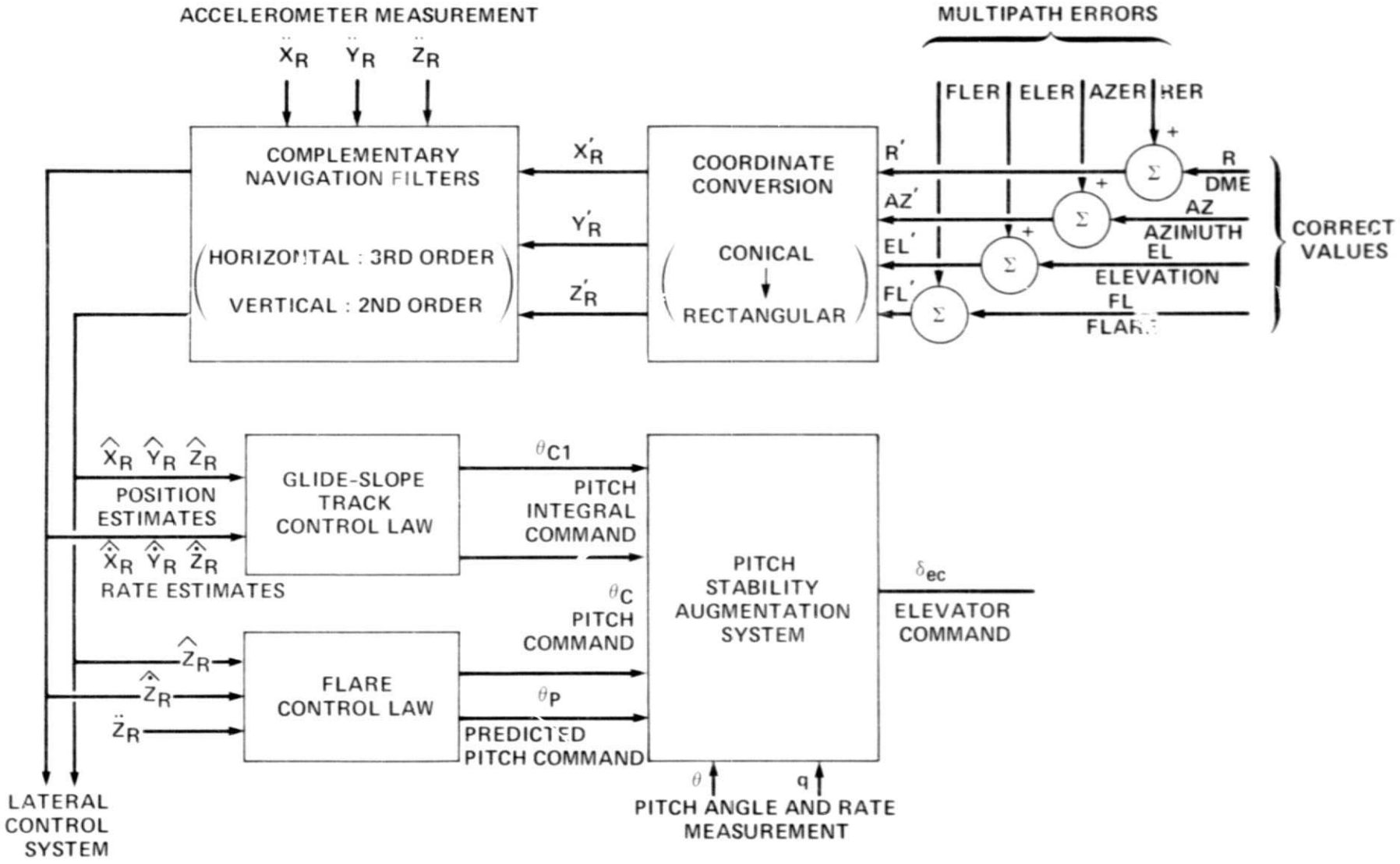

Figure 4.- STOLAND Navigation and Longitudinal Control System.

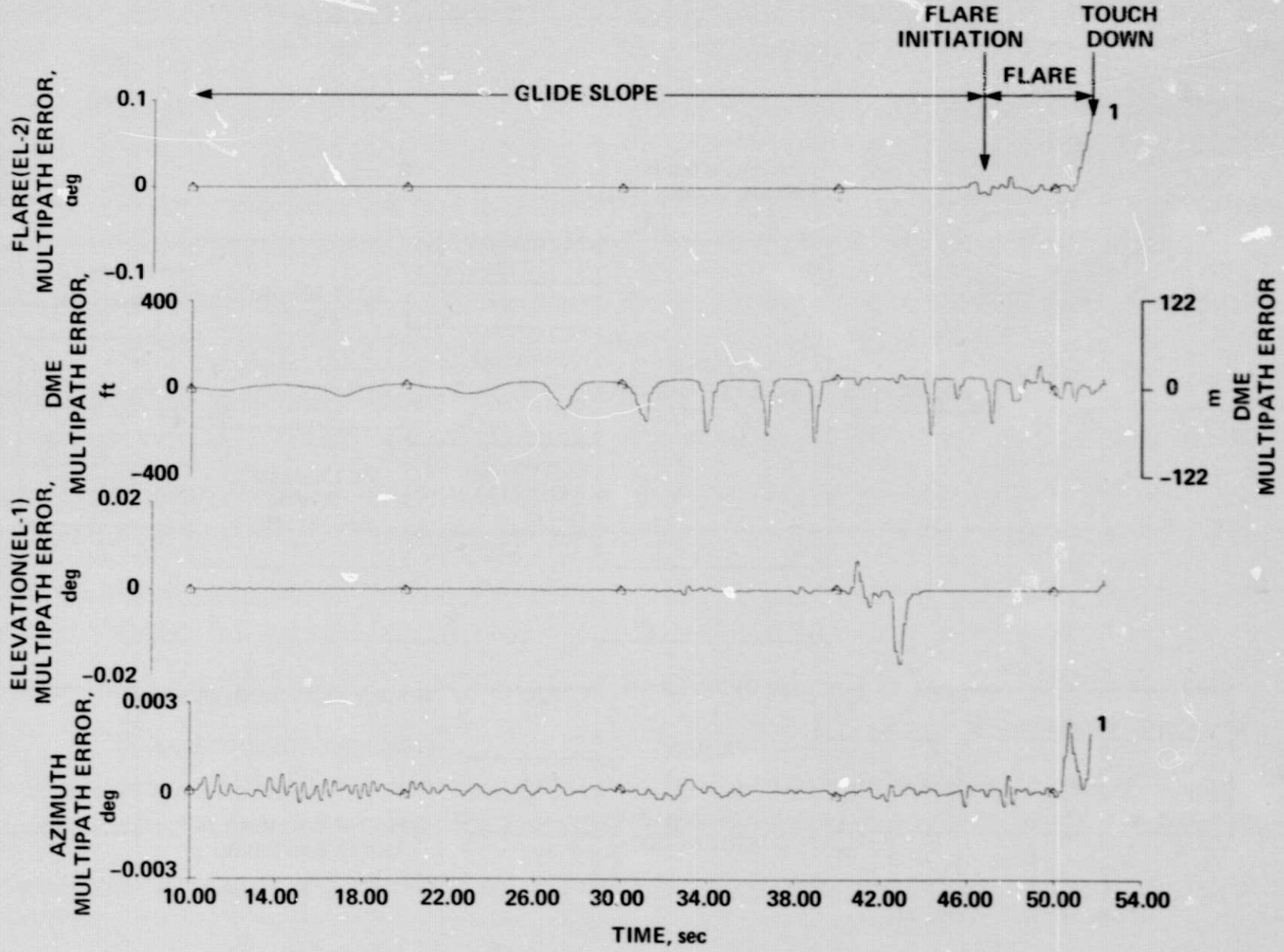

Figure 5.- Crissy Field multipath errors.

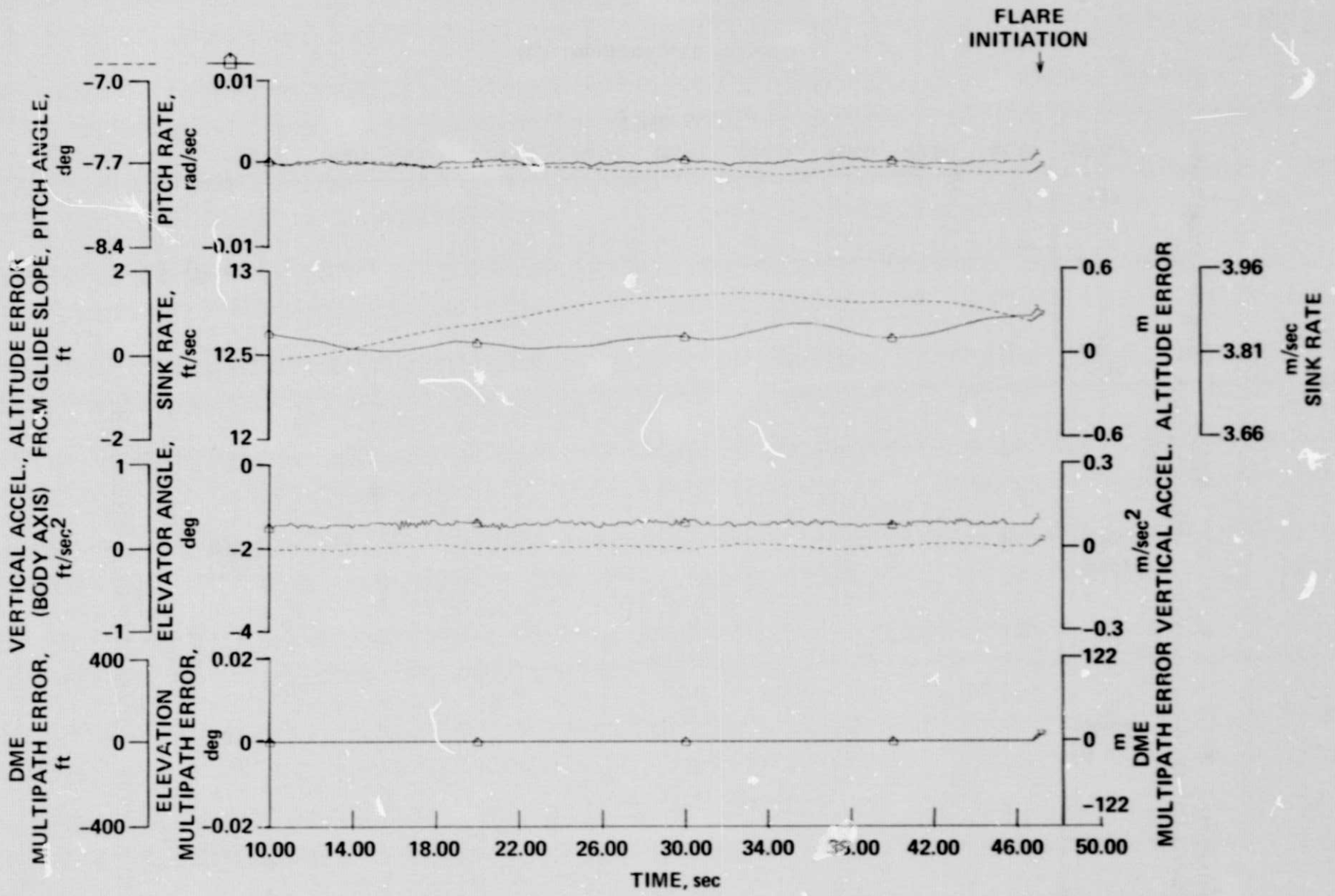

(a) Vertical response

Figure 6.- Aircraft response on glide slope with no MLS errors.

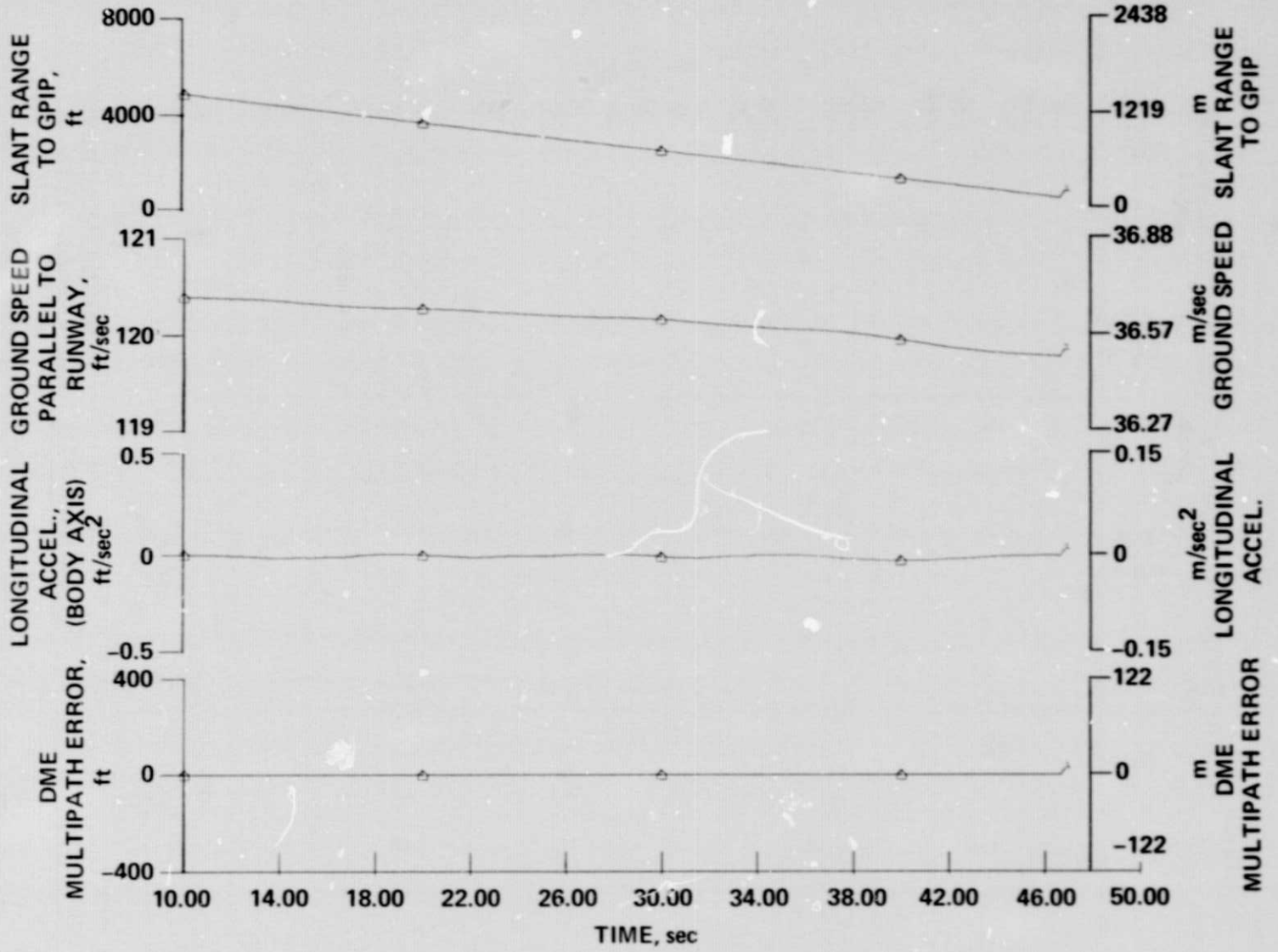

(b) Longitudinal response

Figure 6.- Concluded.

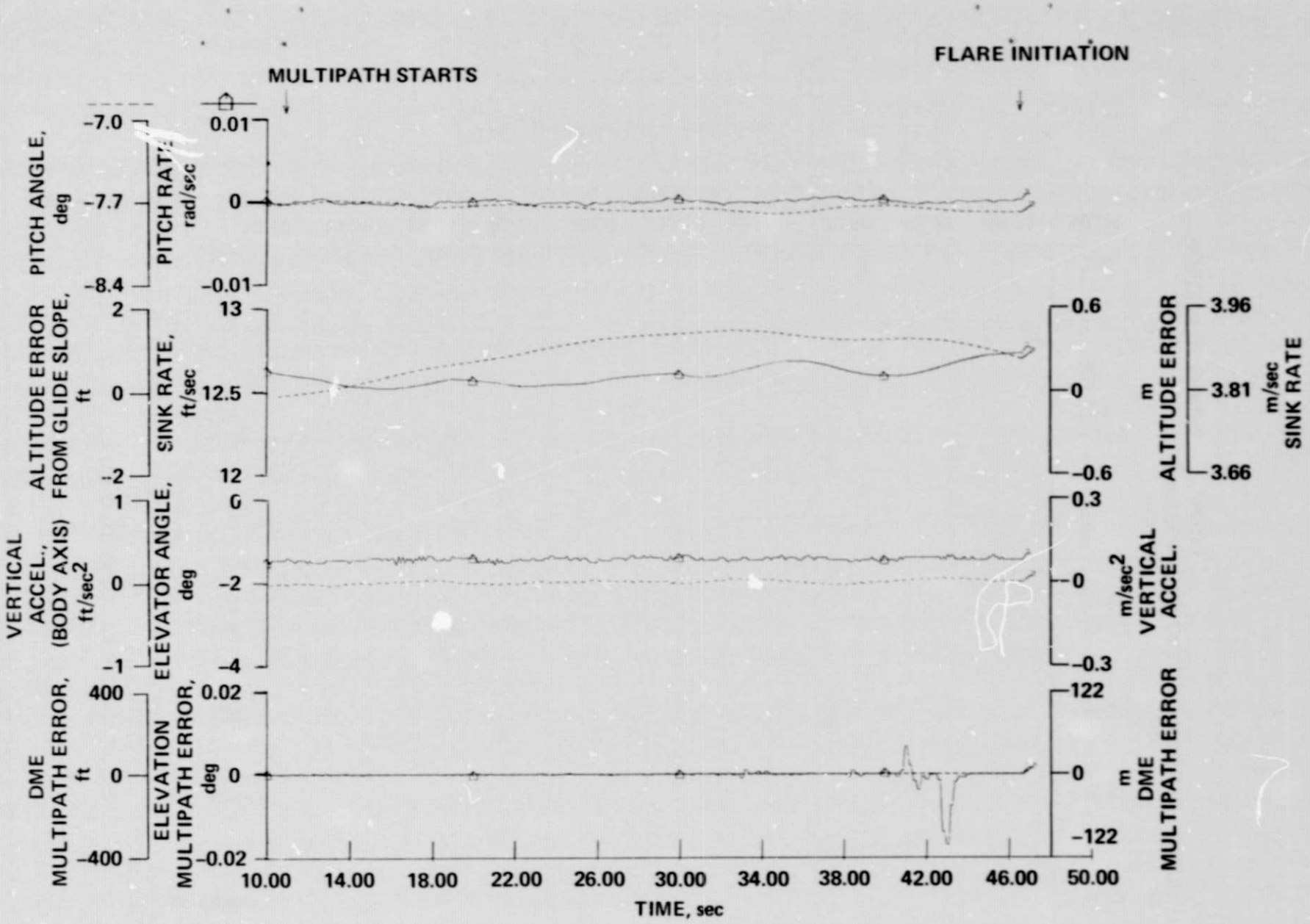

(a) Vertical response

Figure 7.- Aircraft response on glide slope with EL-1 errors.

(b) Longitudinal response

Figure 7.- Concluded.

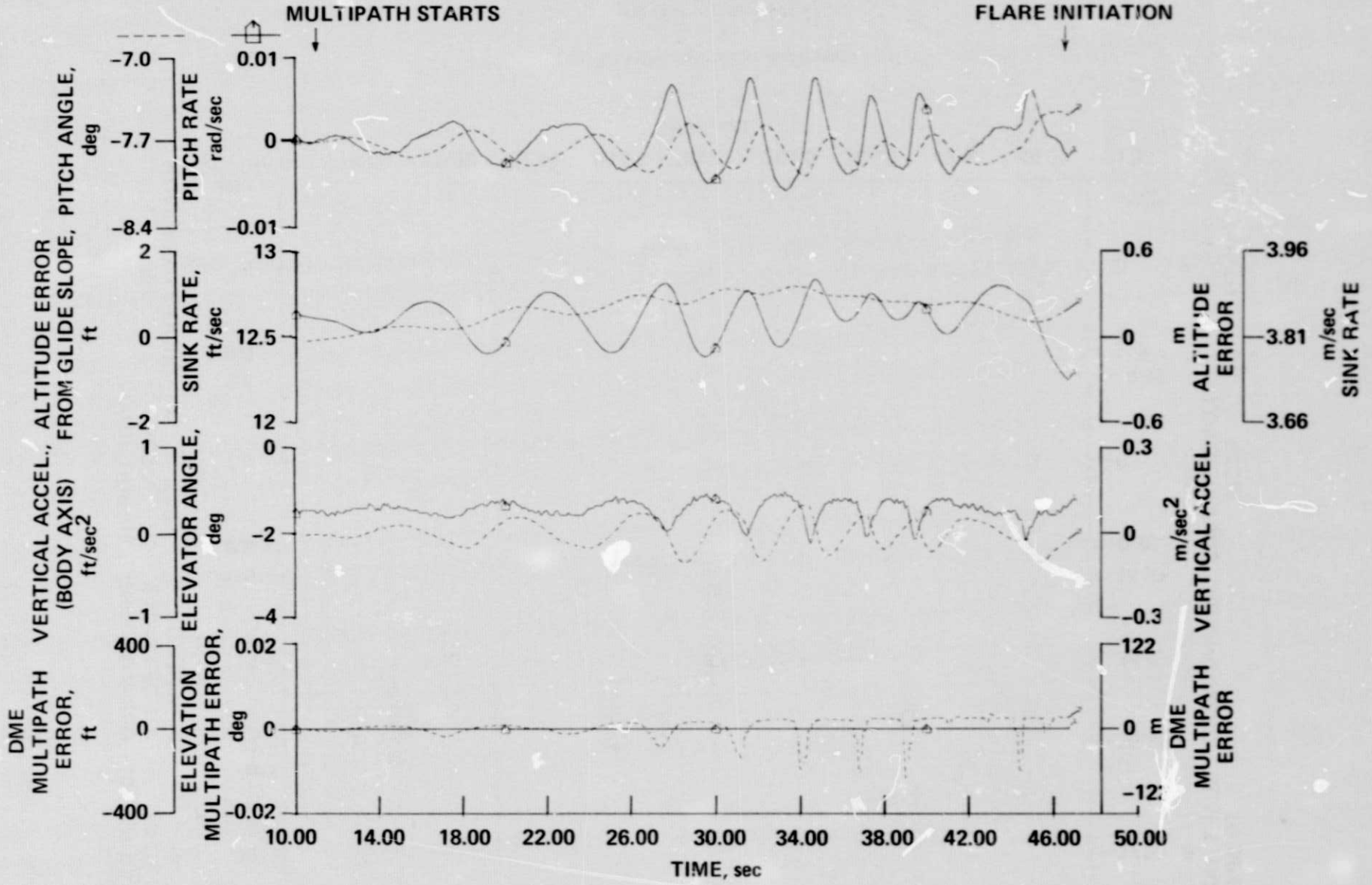

(a) Vertical response

Figure 8.- Aircraft response on glide slope with DME errors.

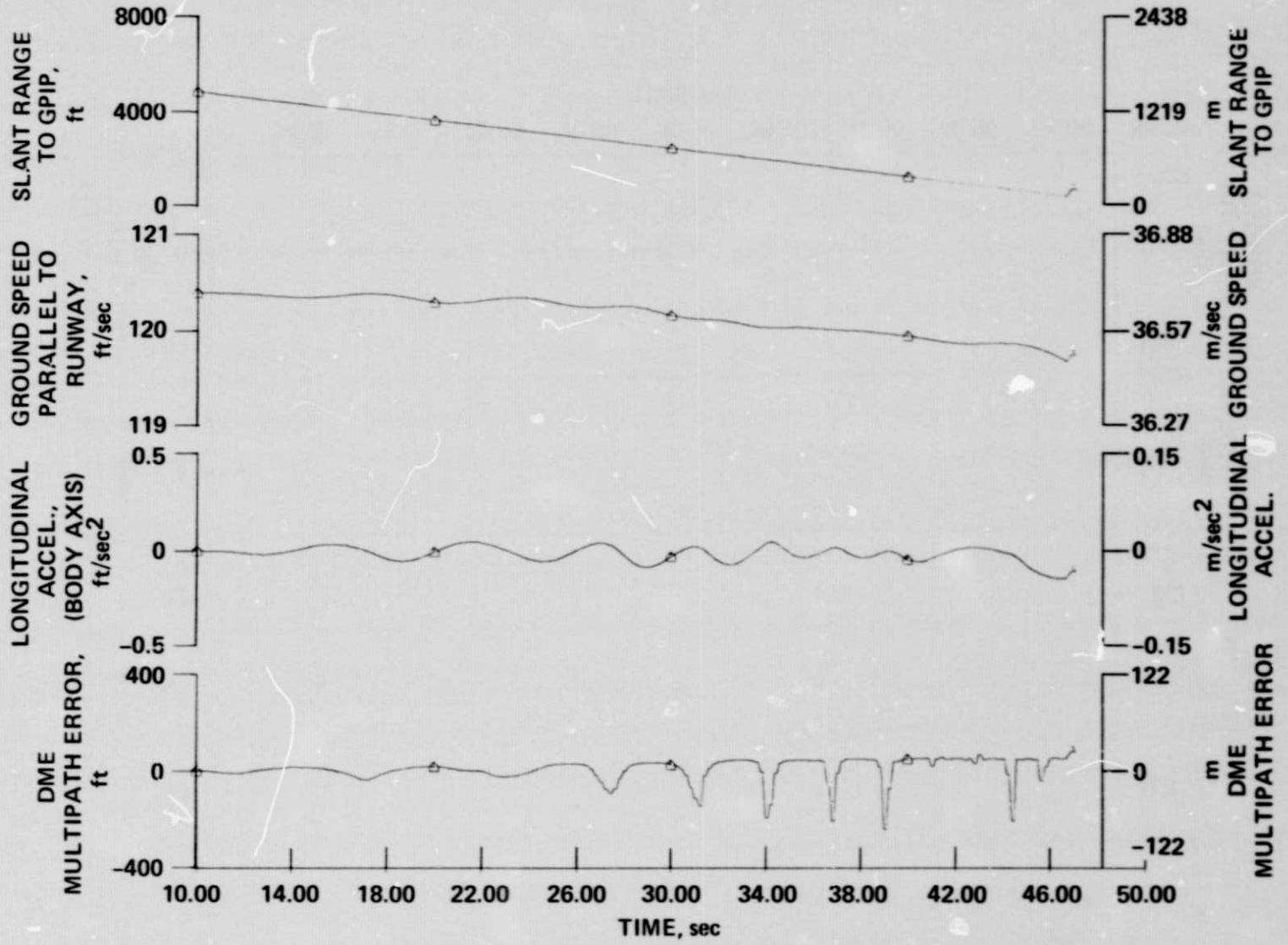

(b) Longitudinal response

Figure 8.- Concluded.

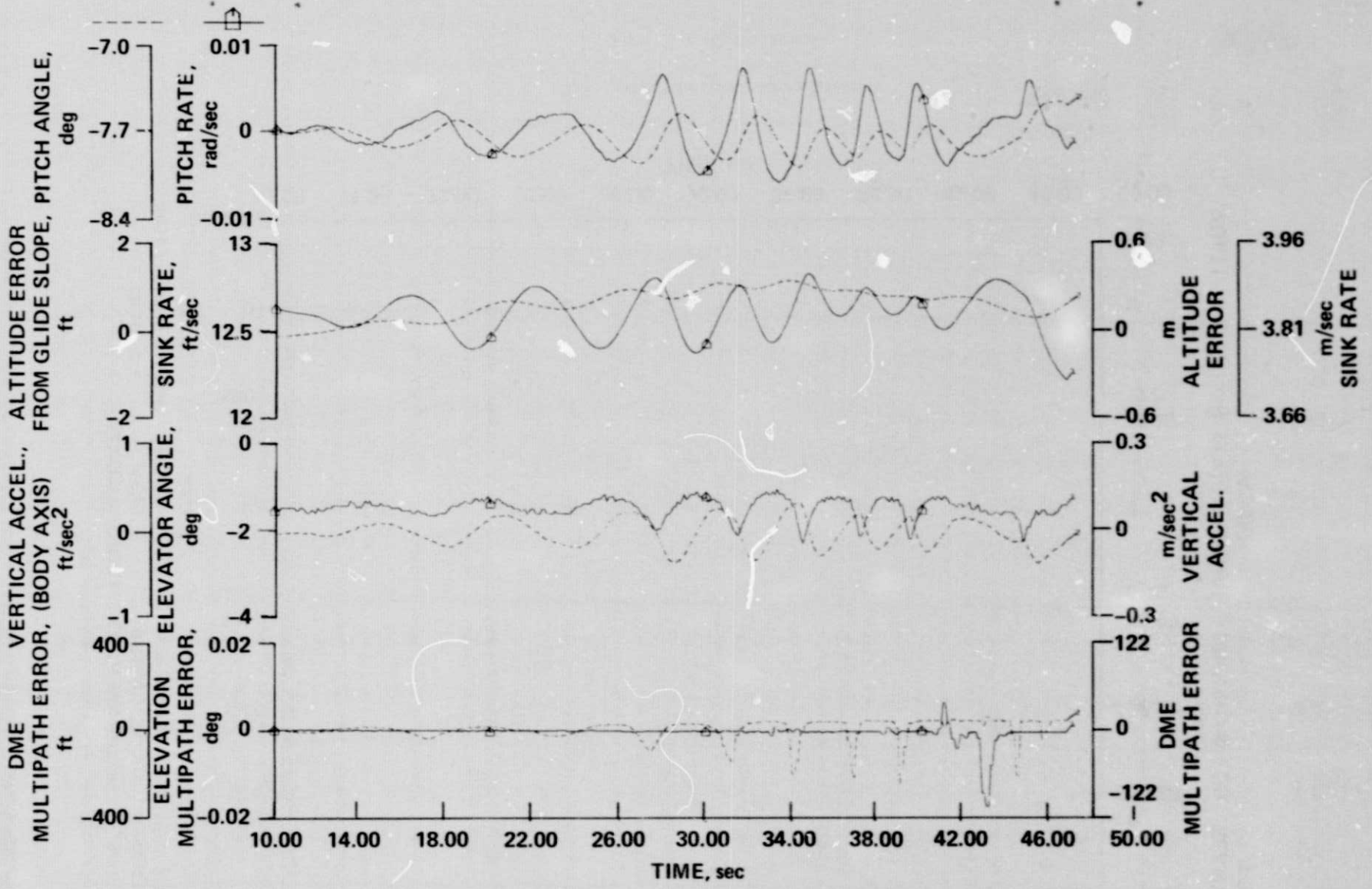

(a) Vertical response

Figure 9.- Aircraft response on glide slope with DME and EL-1 errors.

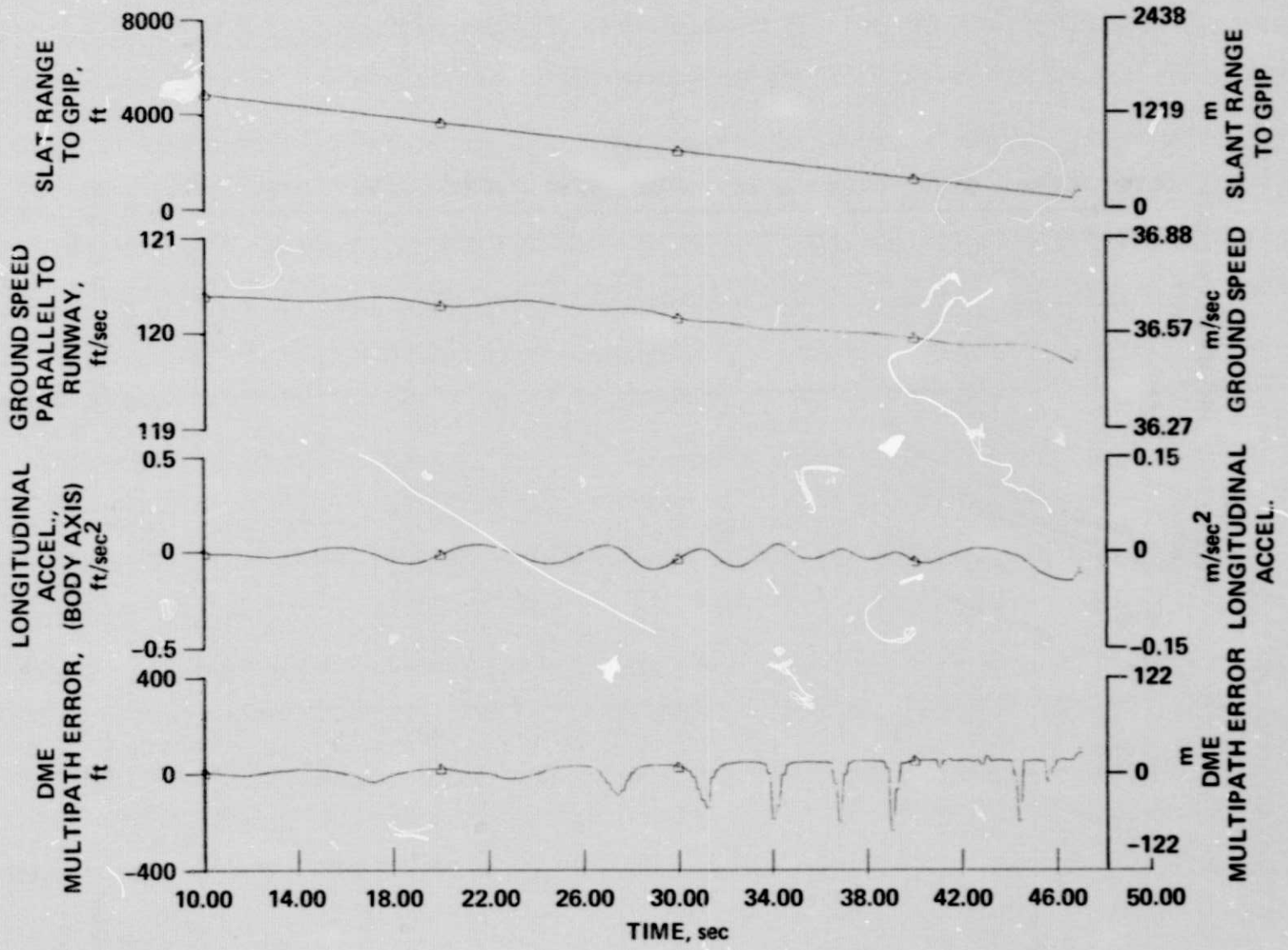

(b) Longitudinal response

Figure 9.- Concluded.

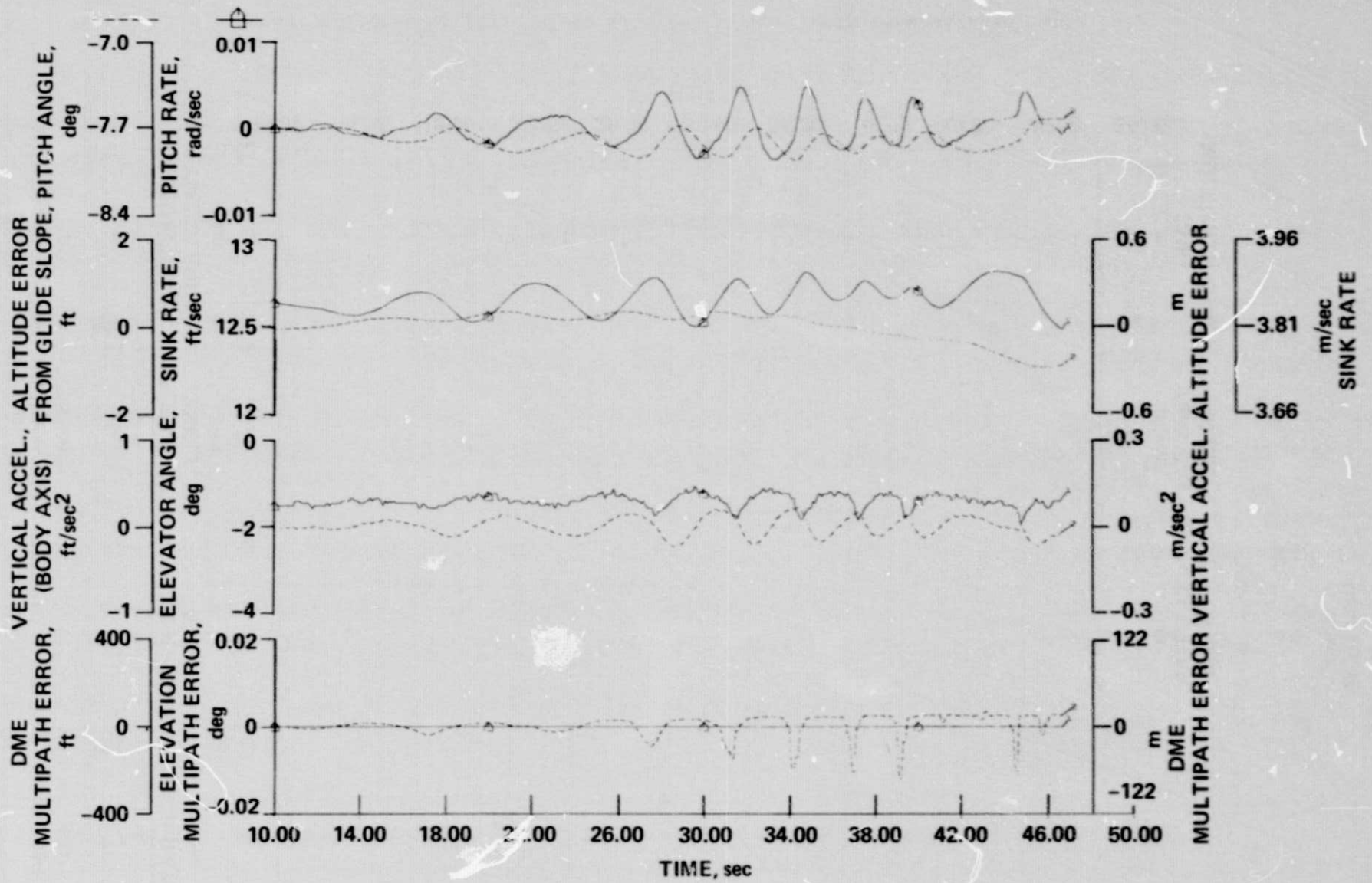

Figure 10.- Aircraft response on glide slope with DME errors (with desensitized navigation filters).

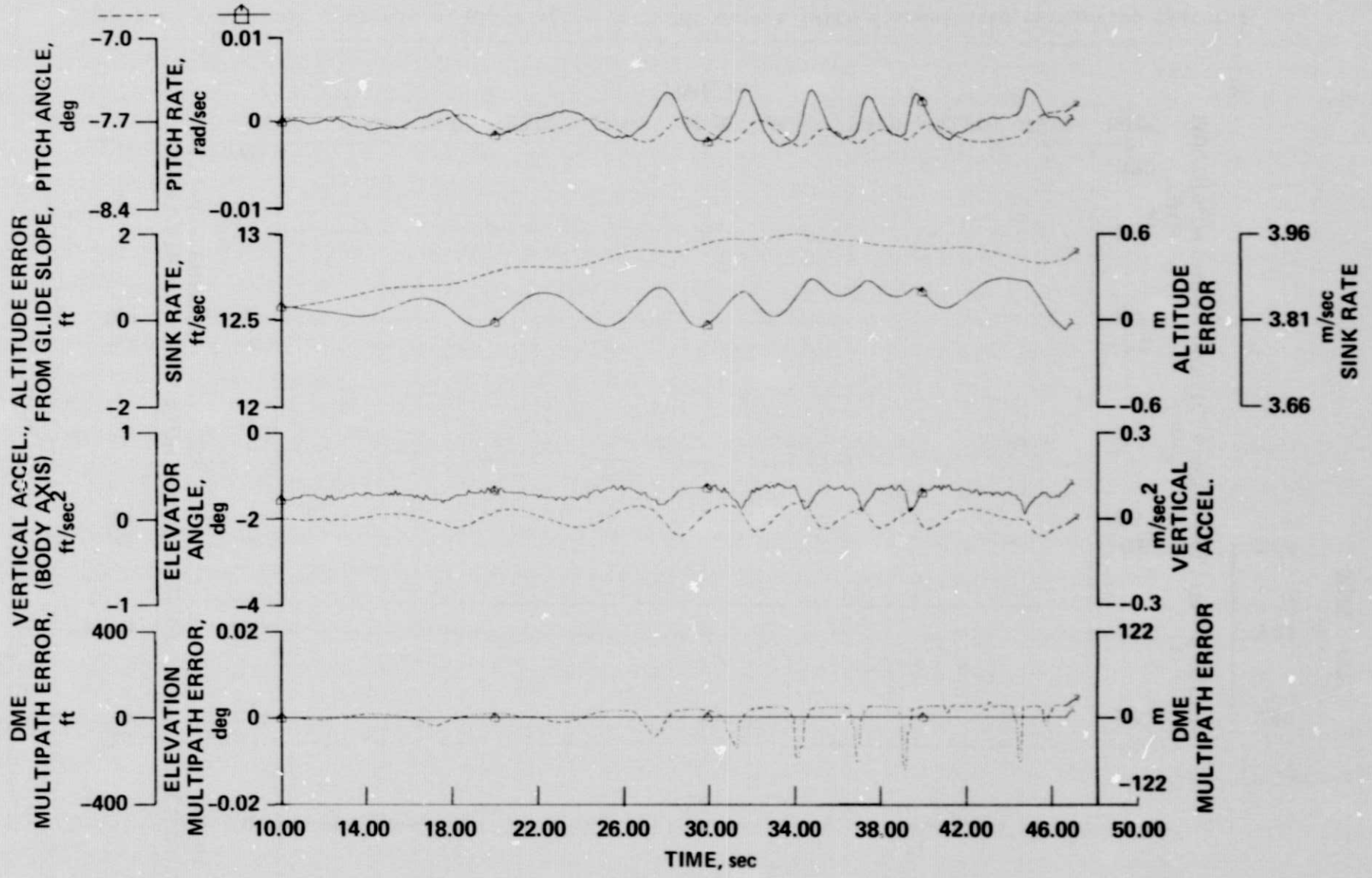

Figure 11.- Aircraft response on glide slope with DME errors (with desensitized autopilot).

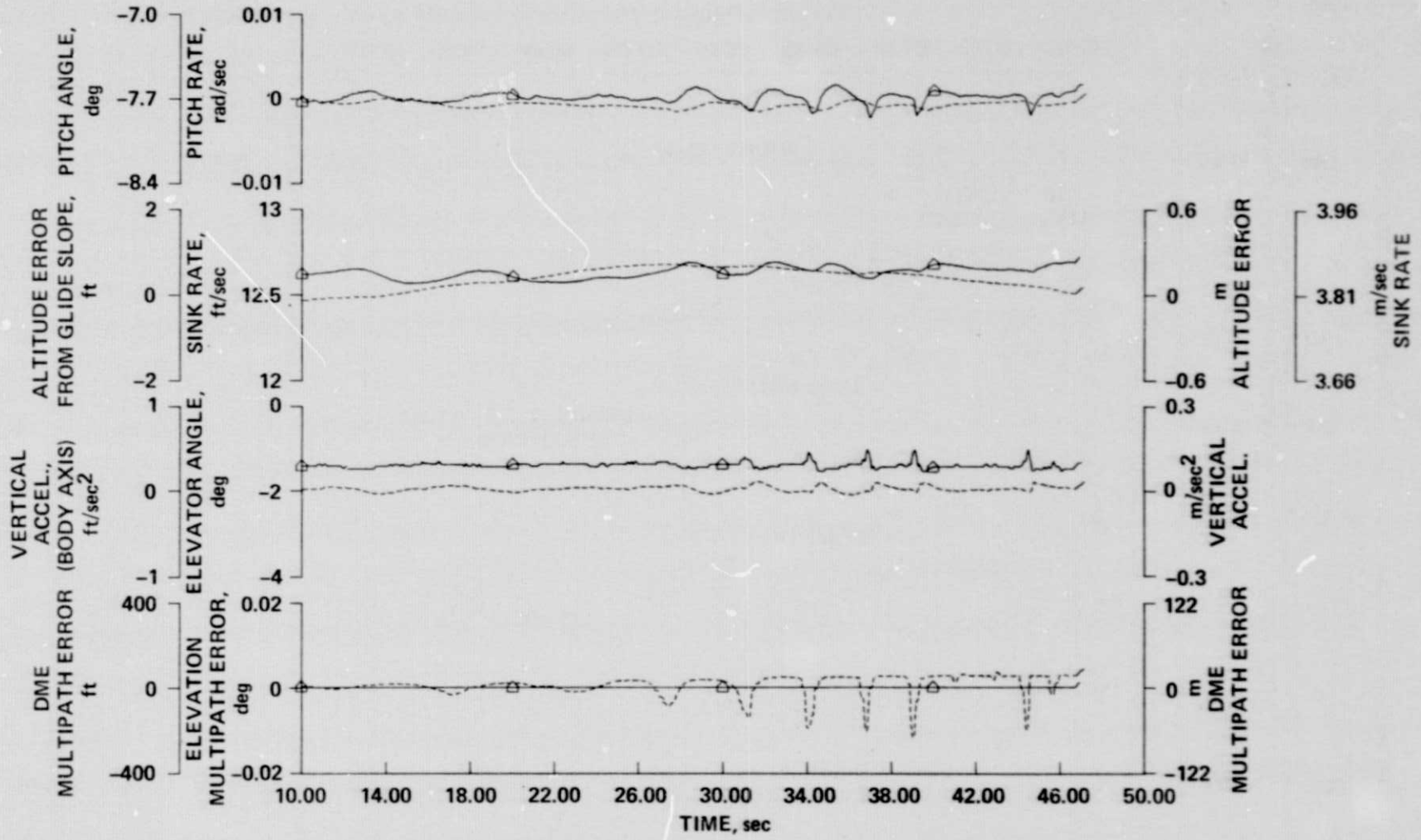

Figure 12.- Aircraft response on glide slope with DME errors (with glide-slope tracking filter).

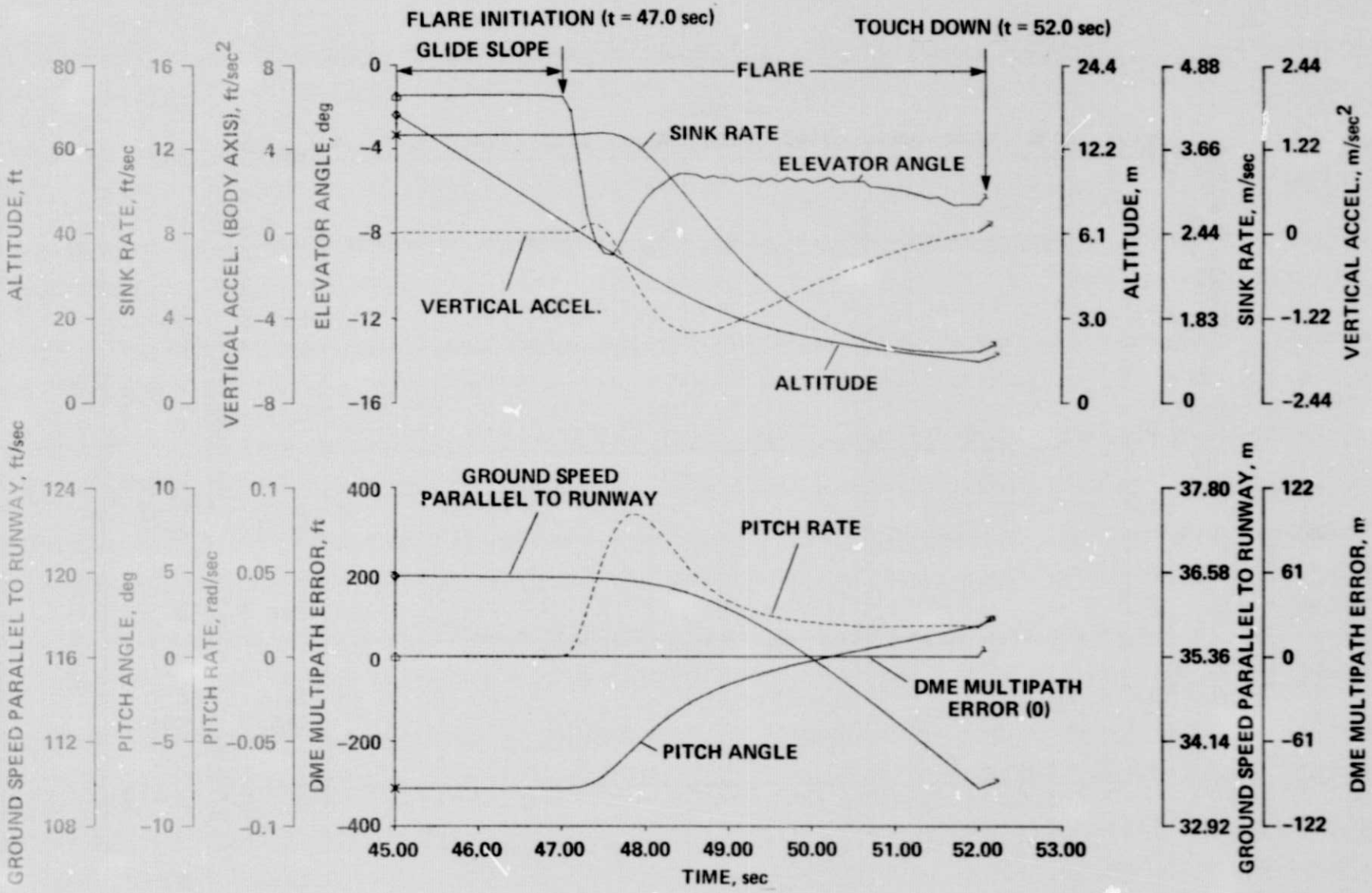

Figure 13.- Aircraft response during flare with no MLS errors.

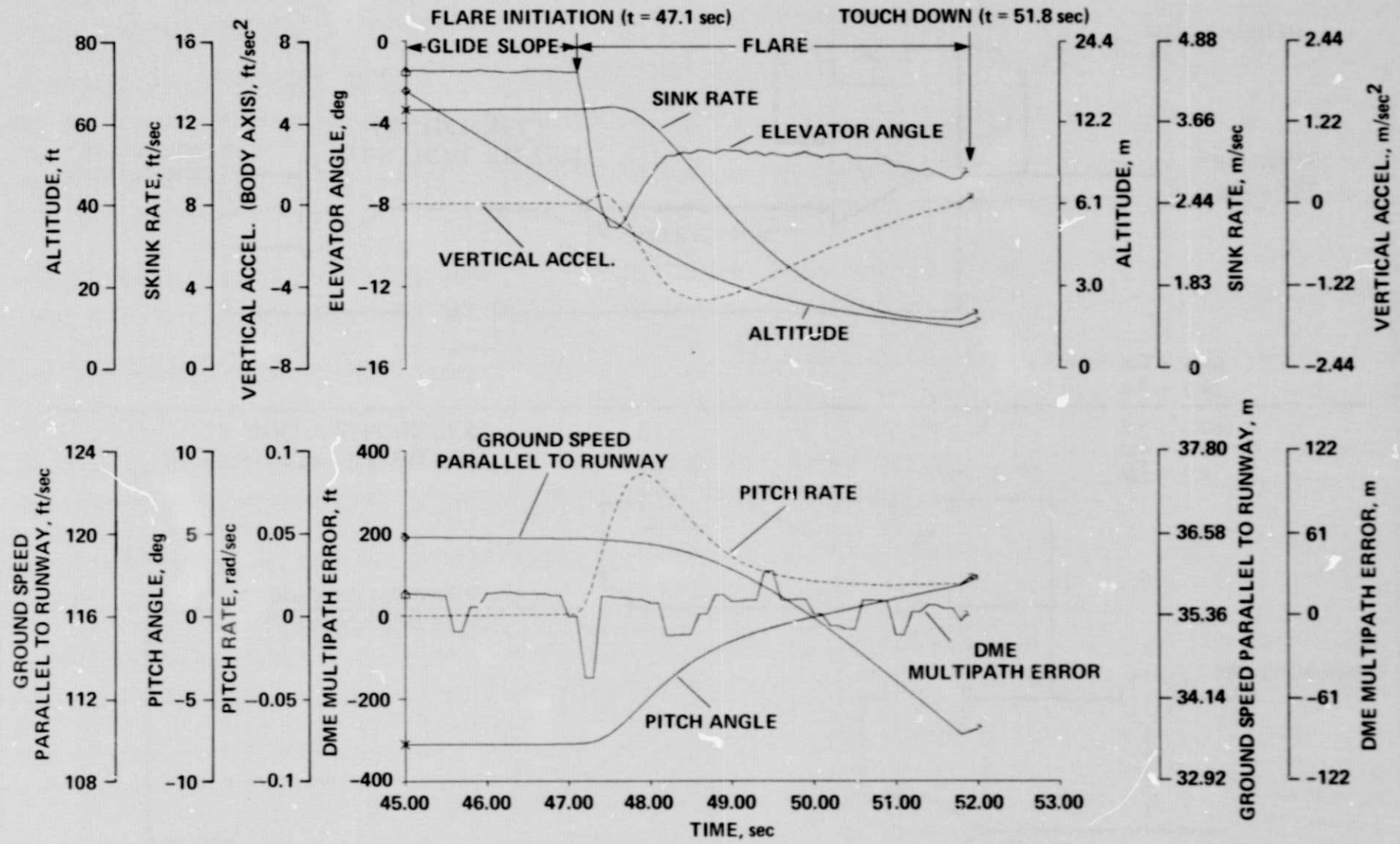

Figure 14.- Aircraft response during flare with DME errors.

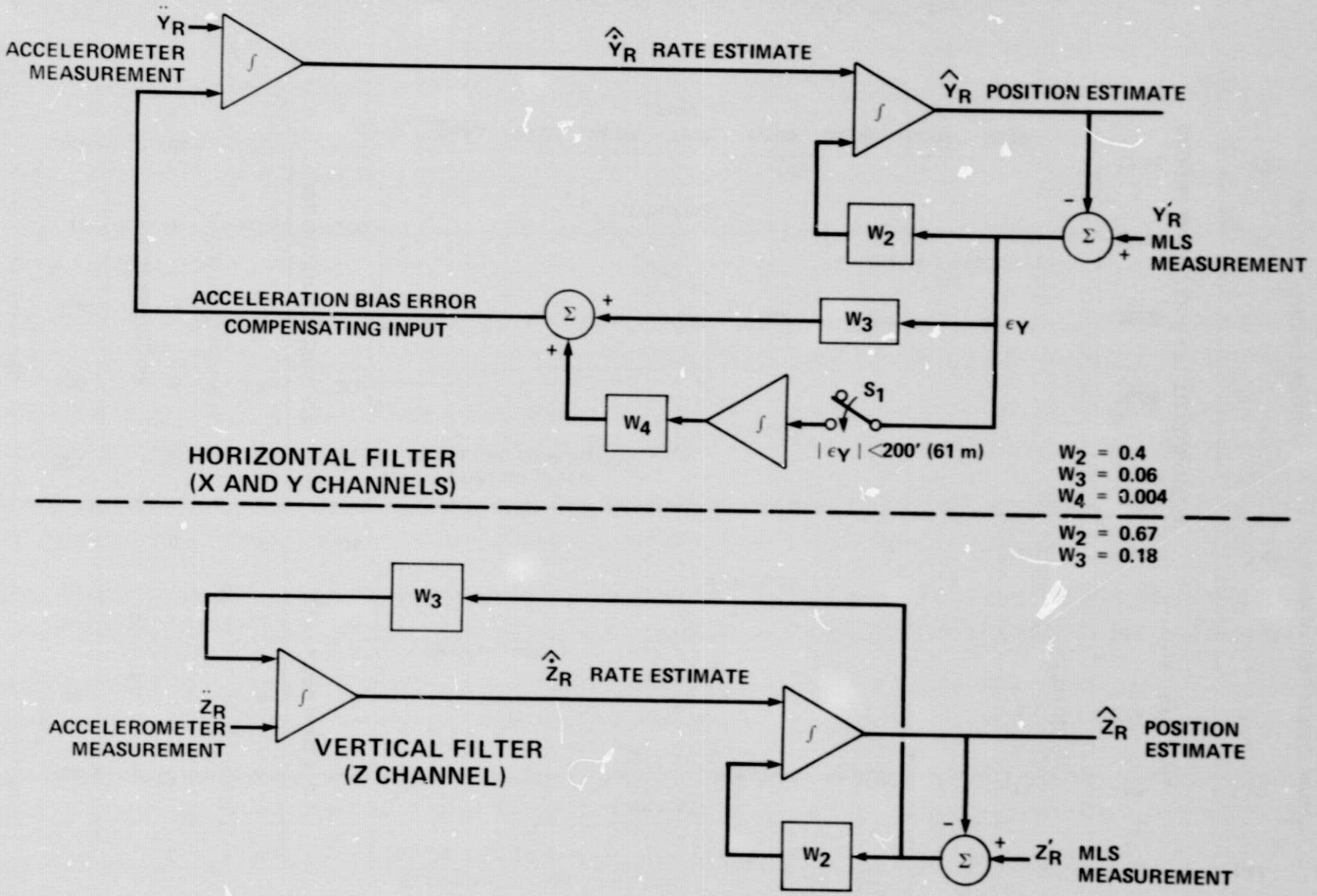

Figure 15.- Navigation filters.

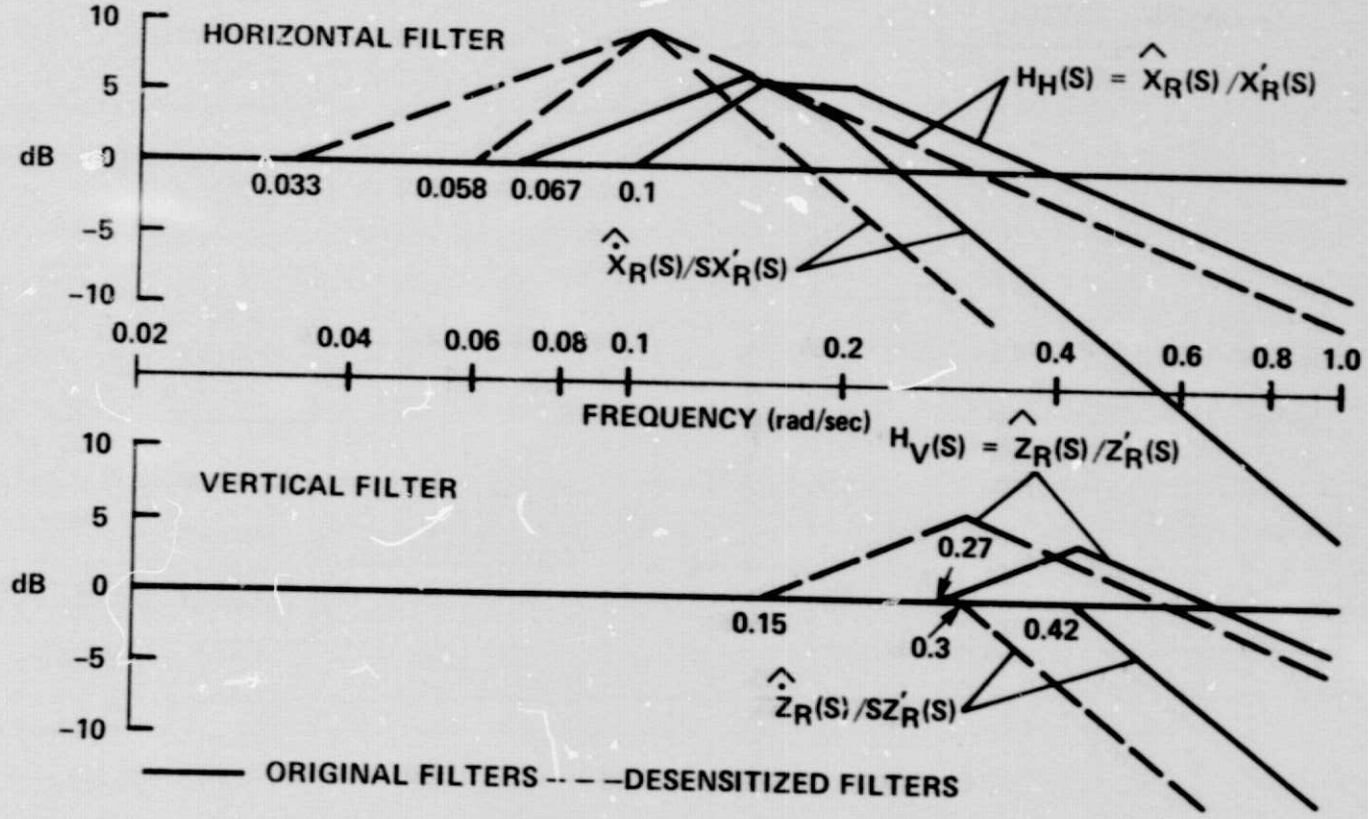

Figure 16.- Navigation filter frequency response.

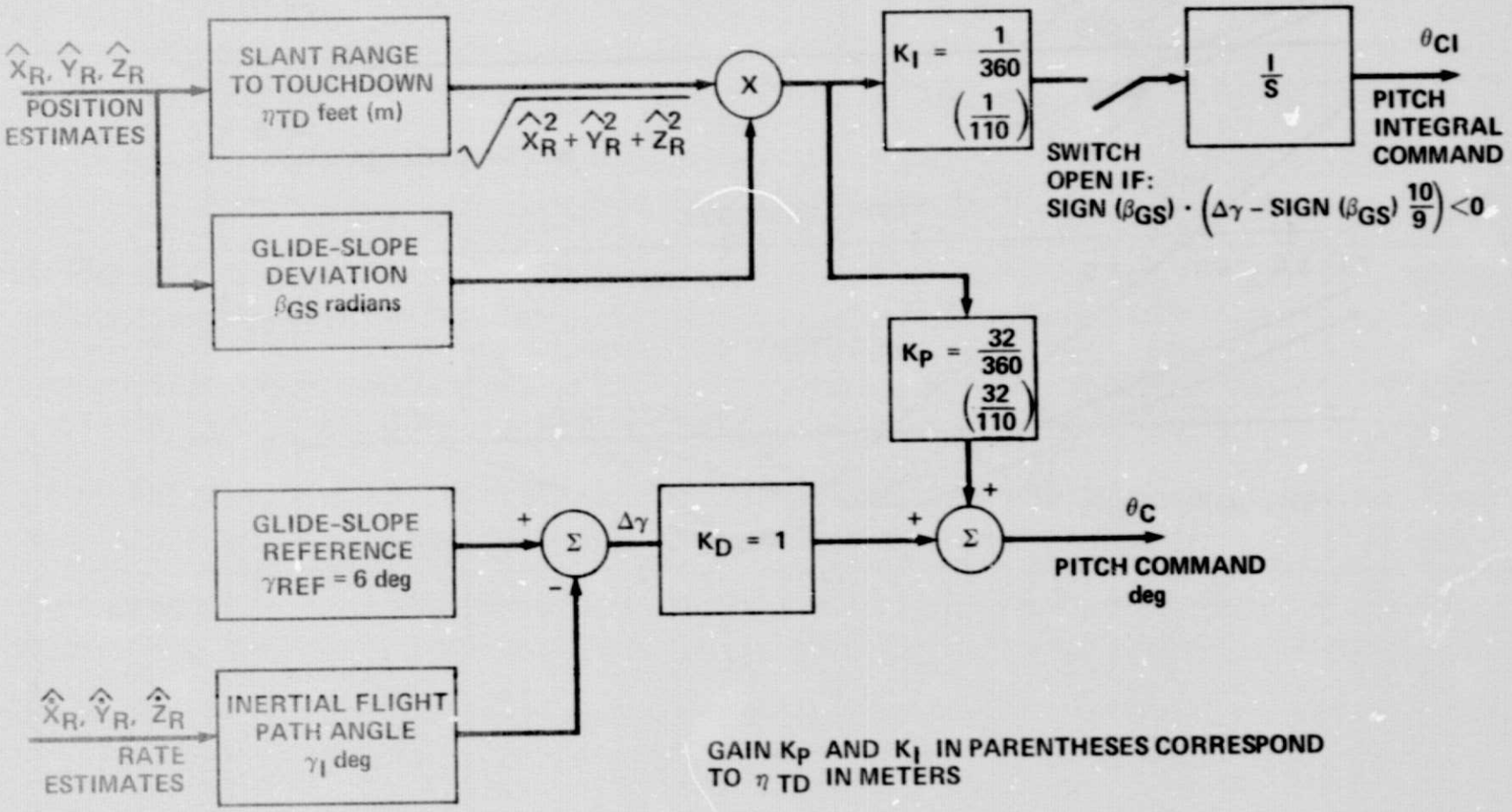

Figure 17.- Glide-slope track control law.

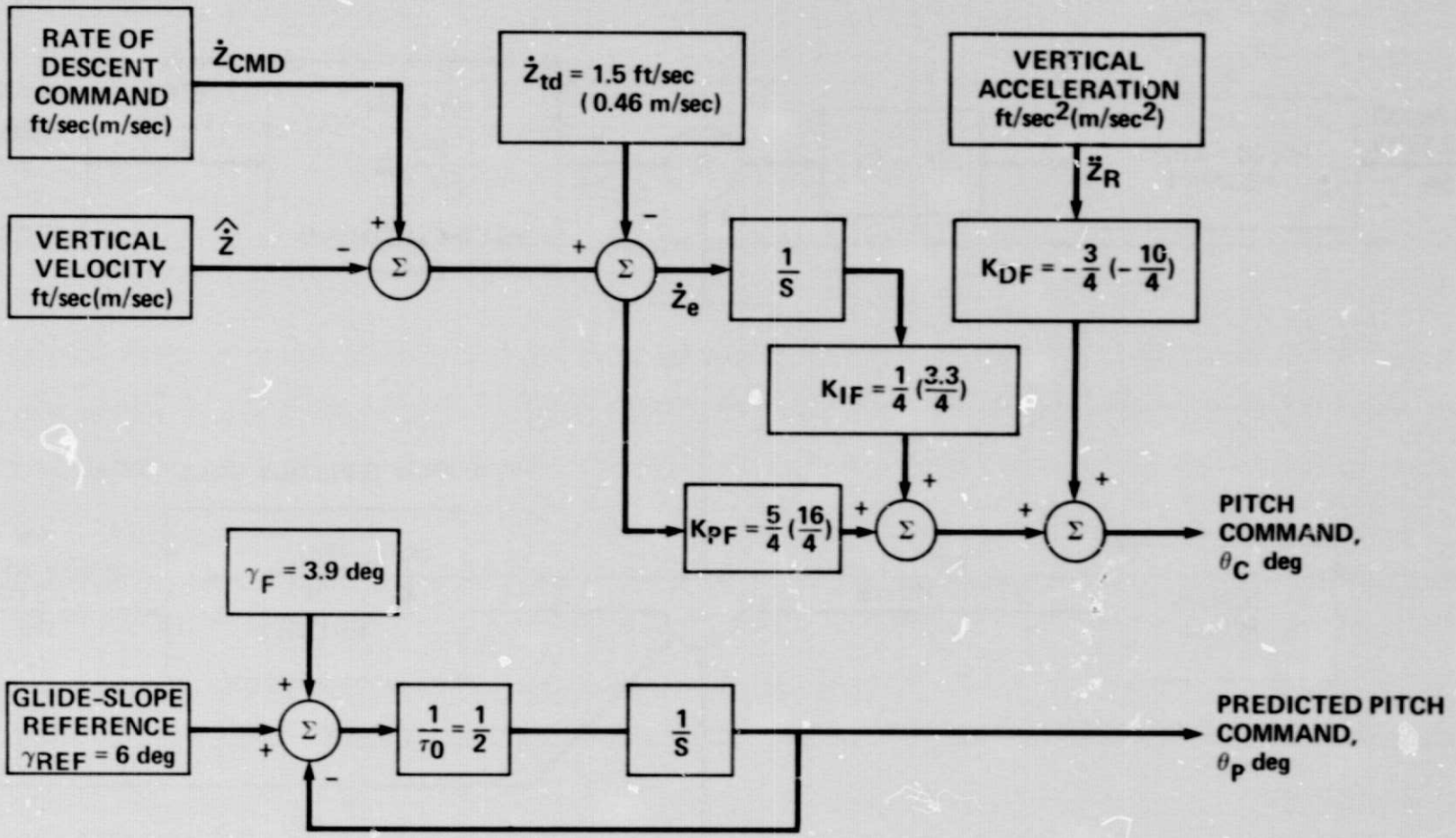

GAINS K_{PF}, K_{IF} AND K_{DF} IN PARENTHESES CORRESPOND TO INPUTS IN METRIC SYSTEM

Figure 18.- Flare guidance control law.

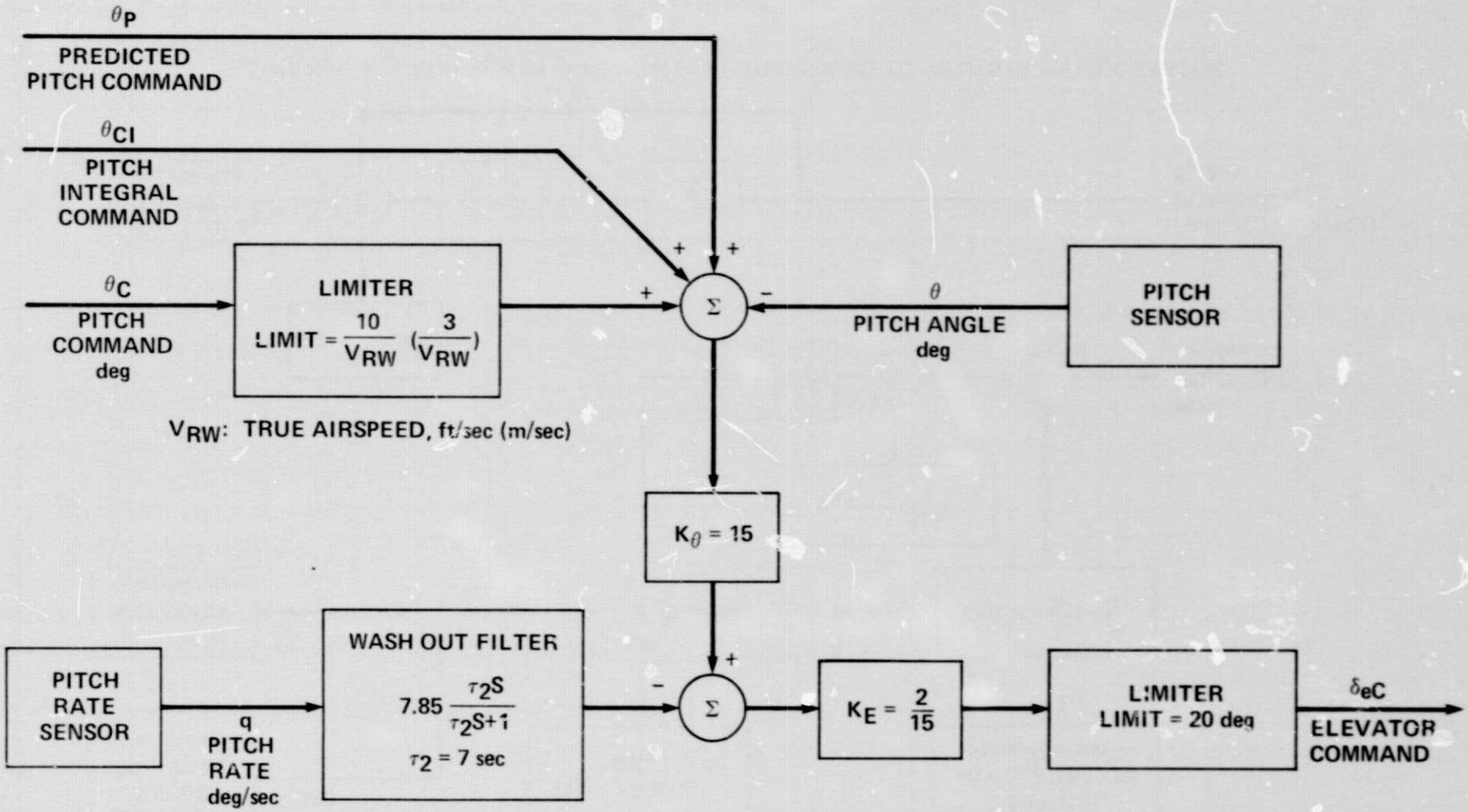

Figure 19.- Pitch Stability Augmentation System.

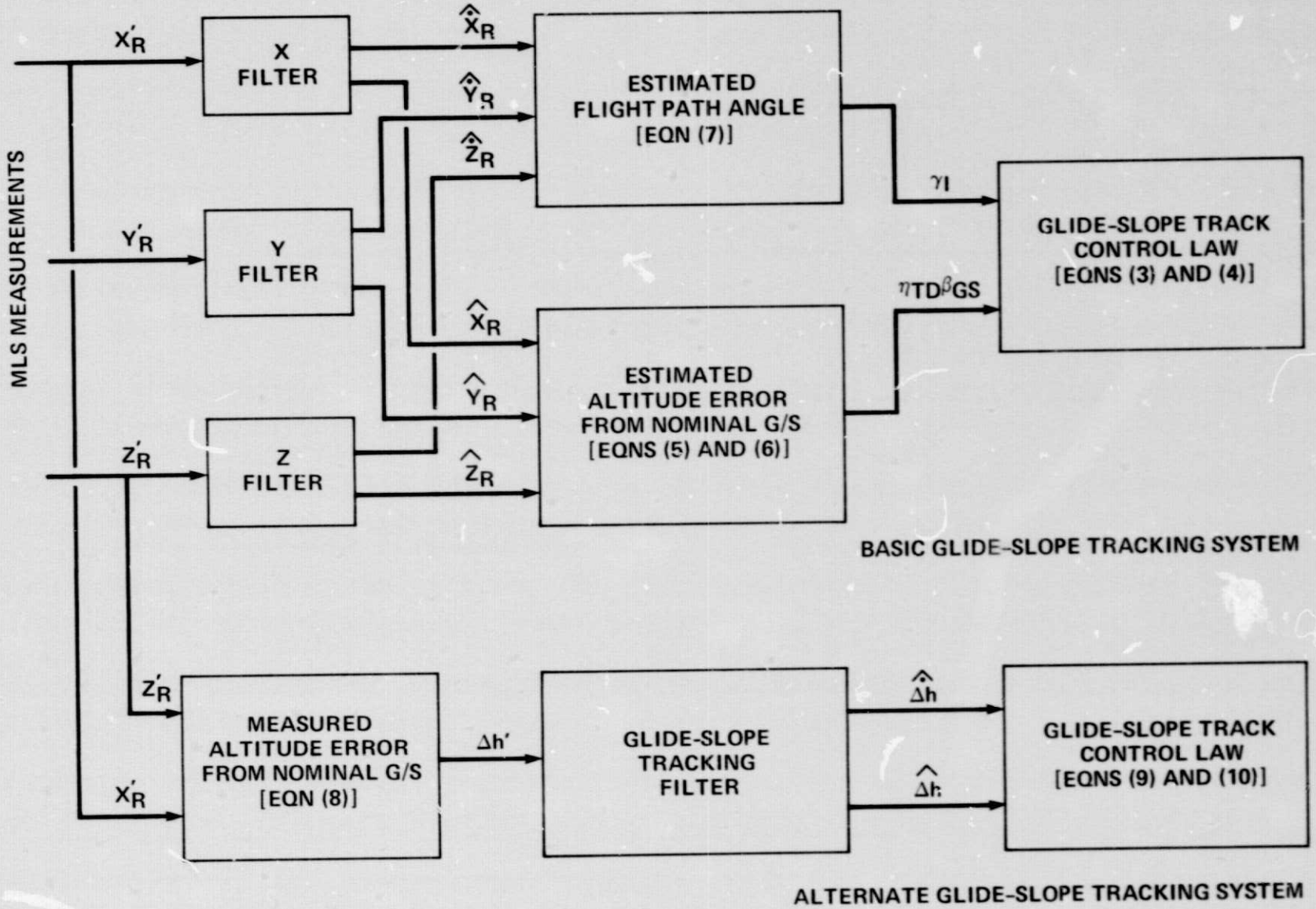

Figure 20.- Comparison of two glide-slope tracking systems.